THESIS

INVESTIGATION OF OPTICAL PRECHAMBER SPARK PLUG AND DUAL LASER PULSES FOR IGNITION

Submitted by

Frank C. Loccisano

Department of Mechanical Engineering

In partial fulfillment of the requirements

For the Degree of Master of Science

Colorado State University

Fort Collins, Colorado

Spring 2011

Master's Committee:

Advisor: Azer P. Yalin

Anthony J. Marchese
Jacob L. Roberts

ABSTRACT OF THESIS

INVESTIGATION OF OPTICAL PRECHAMBER SPARK PLUG AND DUAL LASER PULSES FOR IGNITION

Laser ignition has the potential to increase efficiency and reduce pollutant emissions of natural gas engines. The work presented in this thesis focuses on investigate the reasons behind lower indicated mean effective pressures (IMEPs) obtained in laser ignition tests of Caterpillar G3516C engine when operated with hollow core fibers, and experimentally investigating the effect of using dual laser pulses to increase the total amount of energy deposited in a laser spark. To address the low IMEP, succinct tests were performed on the Caterpillar G3516C engine with a non-fueled electric prechamber plug, a non-fueled laser prechamber plug, and an open chamber laser plug. Test data showed that the open chamber laser plug exhibited a high degree of combustion instability, while the prechamber electrical and laser plug showed similar (improved) performance with the prechamber laser plug having a slightly higher degree of combustion variability. Computational fluid dynamics (CFD) was performed to examine the turbulent flow inside the optical prechamber. The CFD found that to optimize the use of the optical prechamber the spark should be located in the bottom half of the prechamber to reduce the quenching due to turbulence. Bench top

experiments were also performed to examine the possibility of increasing the energy in the laser spark by employing dual laser pulses. The first pulse would initiate the spark while the second pulse deposits additional energy into the spark. It was shown that initial spark can absorb 80 to 90% energy of the second pulse if the inter-pulse separation (Δt) is about 20 to 40 nanoseconds. Overall, better understanding of the use of optical prechamber sparkplugs, as well as the use of dual laser pulses to increase the amount of energy deposited into the spark, will aid in the progression of a practical laser ignition system.

TABLE OF CONTENTS

LIST OF FIGURES

LIST OF TABLES

Chapter 1

INTRODUCTION

1.1 Background

When a laser pulse with enough energy is tightly focused by a lens in a medium, the intensity at the focal volume exceeds the breakdown threshold of that medium resulting in plasma (or laser spark). The plasma temperature and pressure in such laser sparks may reach ~100,000 K and 1000 bar respectively [1-3]. Such laser sparks are commonly used in Laser Induced Breakdown Spectroscopy (LIBS) [4-7] and also as a source of ignition (laser ignition) [1, 8-13]. Studies have shown that laser ignition can operate engines at leaner fuel-air mixtures and higher brake mean effective pressures (BMEP) conditions resulting in reduced emissions and increased efficiency making it an attractive ignition technology for future gas engines [1, 8-15].

1.1.1 Current Ignition Technology in Natural Gas Engines

Currently, like other spark ignition engines, natural gas engines are run on conventional electric spark plugs. However, to increase engine efficiency and decrease oxides of nitrogen (NO_x) in the engine exhaust, the engines need to be run at higher BMEP levels and with leaner fuel-air mixtures [14]. Lean operation leads to a reduction in NO_x production due to lower flame temperatures [16]. However, it can also lead to increased misfires and reduced power output if the ignition source is not reliable (i.e., if the ignition system cannot ignite the fuel-air mixtures consistently) [17]. Hence, a key issue for reliable operation of engines operating at lean conditions (and high BMEP levels) is the performance and reliability of the ignition system [14, 17]. With a standard conventional electrical ignition system, the voltage required to create sparks between the electrodes increases as BMEP increases [14] (i.e., as the in-cylinder pressure at time of ignition increases). The higher voltage requirements can lead to degradation of the dielectric surrounding the ignition wires [13, 14]. Furthermore, higher electrode voltages lead to rapid erosion of the electrodes resulting in increased electrode gap [13, 14] which requires yet higher voltages for breakdown. The high voltages required at these challenging conditions can lead to high strain on the ignition system affecting its overall service life. Herdin et al. reported a 50% drop in service life of the ignition system when BMEP of a test engine was increased from 17 to 22 bar [14]. Obviously, conventional electrical ignition systems are not suitable for next generation high BMEP low emission engines.

On the other hand, laser ignition becomes easier as in-cylinder pressure increases (i.e., at high BMEP) [13], and allows ignition of leaner fuel-air mixtures than is possible with conventional electrical ignition systems [18]. Furthermore, unlike in conventional ignition, there is no quenching by adjacent electrodes and one can locate the laser spark at optimum positions within the engine combustion chamber.

1.1.2 Overview of Laser Spark Physics

There are two main ways by which laser sparks can be generated: resonance enhanced multi-photon ionization (REMPI) [19] and non-resonant multi-photon ionization [1, 8-13]. The work presented in this thesis is focused on creating laser sparks by non-resonant approaches. The first step in this process is multi-photon ionization of the medium resulting in the release of the first free electrons. For example, the ionization energies for oxygen (O_2) and nitrogen (N_2) are 13.6 and 14.5eV respectively. The fundamental output wavelength of the Neodymium Yttrium Aluminum Garnet (Nd:YAG) laser is 1064 nm corresponding to a photon energy of ~1.2eV. As shown in Fig. 1.1, 13 photons of Nd:YAG light ionize a N_2 molecule to generate a free electron. This multi-photon ionization process is followed by electron cascade (or inverse bremsstrahlung) where, in the presence of the electric field of the laser pulse the free electrons are accelerated and collide with neutral particles generating more ions and electrons resulting in an avalanche of electrons or breakdown [1]. A schematic of the electron avalanche is shown in Fig. 1.2 (a) and (b). Studies have shown that intensities of ~100-300

GW/cm^2 for nanosecond pulses are required to achieve breakdown in air at atmospheric pressure [20-23]. There is a wide scatter in the threshold breakdown intensities which is primarily due to different experimental configurations such as pulse durations, focal spot diameters, temporal profiles etc. [20-23].

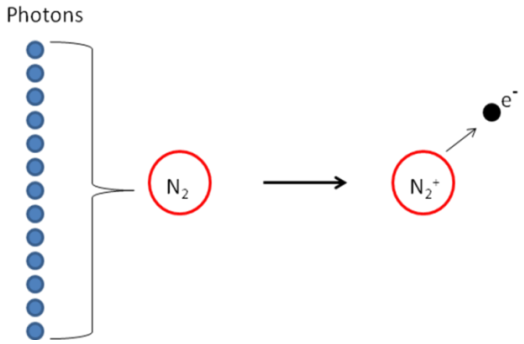

Figure 1.1: Multi-photon ionization of a nitrogen molecule by 1064 nm light.

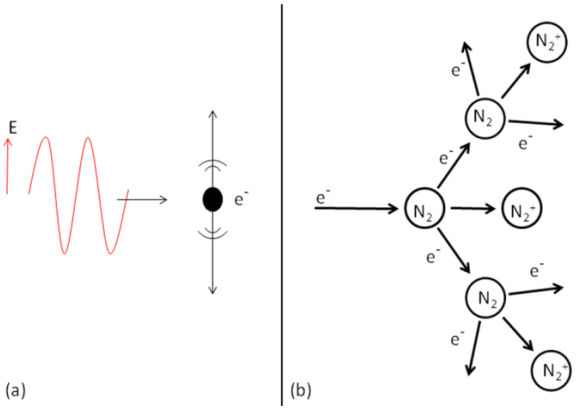

Figure 1.2: (a) Electron oscillating due to electric field of the laser.(b)Electron avalanche in nitrogen environment.

A number of studies have been conducted to characterize the plasma temperature and electron density of laser sparks formed at atmospheric and sub-atmospheric pressures [24-26]. Such laser plasmas have also been characterized in terms of pressure, temperature and electron densities at high

ambient pressures (as of present in engine environments) [27]. For example, in an ambient pressure of 34.5 bar and 3 microseconds after the breakdown, the plasma has a temperature of 13,000 K with electron density of $4x10^{17}$ cm^{-3}. The high plasma temperature aids in providing an effective ignition source.

1.1.3 Benefits of Laser Ignition toCombustion in Natural Gas Engines

There are many potential benefits of using laser ignition in stationary natural gas engines:

A) Reduction in heat loss due to quenching: Since there are no electrodes on an optical sparkplug there is no quenching and the spark can be located at an optimal position away from the engine cylinder walls [16].

B) A second benefit comes from the higher flame speeds of (early) flame kernels formed by laser sparks as reported by Bradley et al. [28]. As shown in Figure 1.3, the laser spark (or flame kernel) has faster laminar flame speed (S_n) compared to electric sparks at early times of the flame kernel evolution. Note that time increases to the right in Fig. 1.3. Such faster flame speed makes the kernels more resistant to quenching due to turbulence and hence may reduce ignition delay.

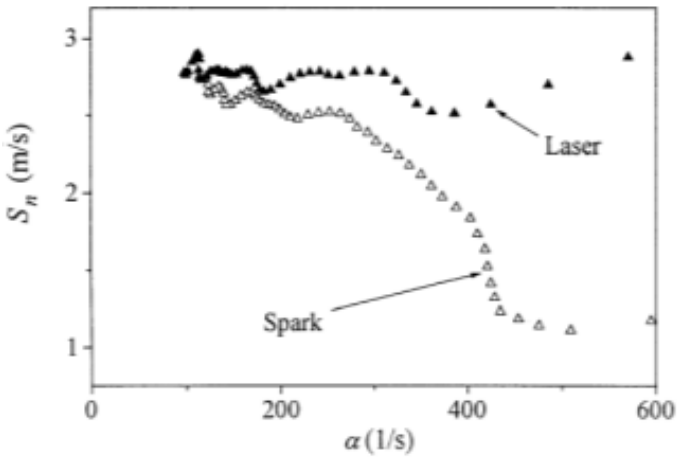

Figure 1.3: Comparison of flame speed for laser andelectric spark ignition. Time is from right to left on the horizontal axis. [28]

C) Reduced breakdown intensity at high pressures: As briefly discussed in Section 1.1.1, for lean fuel-air mixtures,as the in-cylinder pressure increases, the voltage applied to the spark plug has to be increased to achieve breakdown (or spark). However, higher voltages results in rapid electrode erosion and eventual breakdown of the ignition system [14]. On the other hand, laser ignition becomes progressively easier as the in-cylinder pressure is elevated [15, 29]. As shown in Figure 1.4,Sircar et al. the breakdown threshold intensity decreases with increasing ambient pressure, as a result of greater degree of collisional ionization[30].For example, at 100 torr, 500 GW/cm^2 is required to create breakdown, versus 200 GW/cm^2 at 600 torr. Hence, for a given focal area, lower laser energy is required to create sparks at higher pressures.

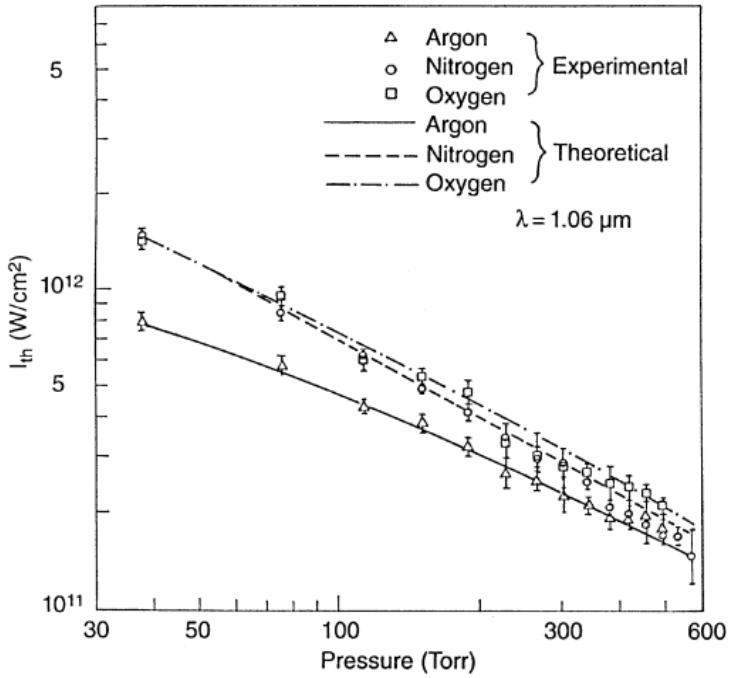

Figure 1.4: Intensity threshold versus pressure[30].

D) Extension of Lean Limit: Studies have shown that engines running with lean air-fuel mixtures (i.e., higher air-fuel ratios) result in lower NO_X production due to lower in-cylinder flame temperatures [17]. However, at higher air-fuel ratios combustion efficiency starts to decreases due to misfires resulting from the inability of the electric spark plugs to reliably ignite the mixtures [14]. The air-fuel ratio beyond which the combustion efficiency drops so as to make engine operation unsustainable, referred to as the “lean limit”. It has been shown that increasing speed of the initial flame kernel can extend the lean limit[18]. As discussed earlier, laser ignition provides an ability to locate sparks in an optimal location within the combustion chamber (away from quenching sources) and to produce early flame kernels

with higher flame speeds, the result of which is to extend the lean limit beyond that is possible with electric spark ignition. For example, as shown in Fig. 1.5, laser ignition shows the ability of laser ignition to ignite the leanest fuel-air mixtures (air-fuel ratio of ~2.07) in a single cylinder research engine providing the lowest NO_X of ~0.2 g/kWh. In the figure, the green line shows achievable NO_X when the engine is run with direct electrical spark plugs in the main combustion chamber, while the red and blue curves are for engine configuration when combustion is achieved in the main chamber by using prechambers fitted with electrical spark plug. The red and blue curves are for different prechamber volumes. Although, the figure shows only one data point for laser ignition (yellow circular marker) the ability to get NO_X down to 0.2 g/kWh with laser ignition is promising for next generation high BMEP low emission engines.

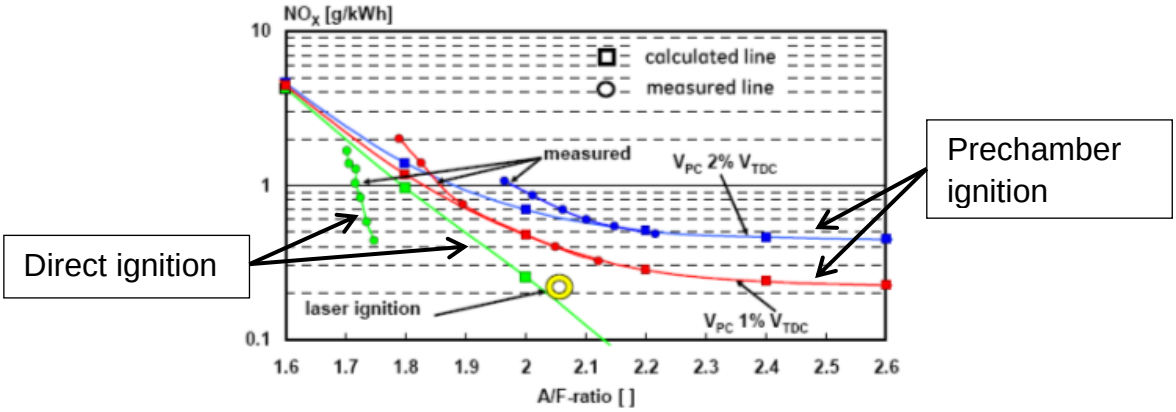

Figure 1.5: NO_X production versus air/fuel ratio. Square markers indicate calculated lines while circle markers indicate measurements for prechamber ignition, and direct ignition. Laser ignition is indicated by the circular marker[18].

E) Optical Combustion Diagnostics: Laser ignition inherently provides a window into the combustion chamber making it possible to collect light from spark or combustion and conduct diagnostics. For example, cylinder and cycle resolved collection of light from combustion can provide information as to the rate of misfires (which is critical for emission control). Similarly, Joshi et al [27] used laser sparks to operate a Co-operative Fuel Research (CFR) engine and simultaneously conduct LIBS. They mapped air-fuel ratios inside the engine cylinder by using the ratios of atomic lines of H_α and O and H_α and N. Such optical combustion diagnostics capability provided by laser ignition can form a critical part of closed loop combustion control of the next generation high efficiency engines.

1.1.4 Minimum Energy Requirements for Ignition at Lean Operation

As discussed in the above sections, laser spark formation requires the beam to be focused to a threshold breakdown intensity. However, for combustion applications, there additionally exists a minimum ignition energy (MIE) required for consistent ignition and combustion. This MIE may correspond to a pulse energy than that is required for sparking. For example, if a 1064 nm laser pulse is focused into a 10μm spot size, then only ~2.5mJ pulse energy (10 ns pulse duration) is required to achieve the breakdown threshold intensity (~280 GW/cm^2). However, as shown in Figure1.6, pulse energies >10 mJ are required for ignition of lean methane-air mixtures with 5% methane (by volume) or less

[29]. (Note that 5% methane by volume corresponds to air-fuel ratio of 20and 10% methane by volume corresponds to stoichiometric air-fuel ratio of 10.5). In the figure, the "+" symbols, black dots, white circles, white squares, and solid line correspond to laser ignition, whereas the dotted line corresponds to electric ignition, and white inverted triangles indicate computations. All the data points are from tests performed at atmospheric pressures except the "+" markers which are from experiments performed at 30 bar. All data show an increase in minimum ignition energy when the air/fuel mixture becomes either lean or rich and the ignition energy is minimum at stoichiometric conditions (9.5% methane by volume). For gas engines of interest, the ignition energy required for ignition and combustion is in the range of 10 – 20 mJ for methane fraction of 5% and less.

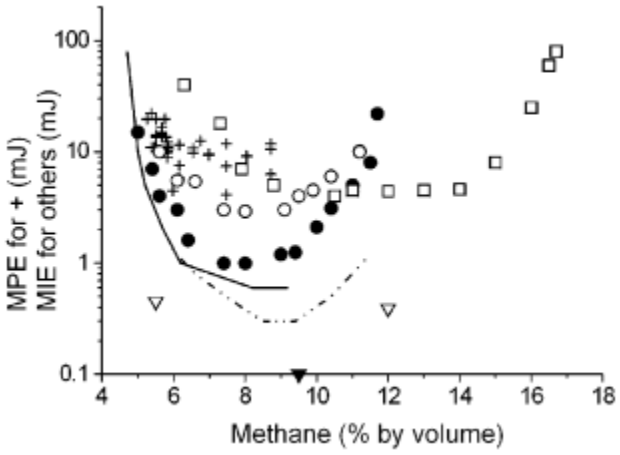

Figure 1.6: Minimum pulse energy (MPE) and minimum ignition energy (MIE) requirements for laser ignition as well as standard electric ignition (dotted line), and computations (white inverted triangles)[29].

1.1.5 Current State of Development of Laser Ignition Technology

Although laboratory tests starting with Dale's experiment in 1979 have shown potential advantages of laser ignition over conventional electric spark ignition, there remain challenges in transferring the technology from the laboratory setup to practical implementation in the field. A primary challenge is the cost of laser ignition which varies for different system architectures. The most obvious system architecture would be the use of a single laser with laser being directed to the engine cylinders via a series of mirrors mounted on the engine. However, such a system is impractical owning to misalignments due to vibration and thermal expansion, potential damage due to harsh engine environments (temperature, dust etc.), and lack of safety.

Currently, there are four candidate architectures for laser ignition system for engines: i) single laser per cylinder [31], ii) fiber delivery of pump light to gain element mounted on individual cylinders [32], iii) multiplexed fiber lasers [33], and iv) a single laser multiplexed into different engine cylinders via passive optical fibers [8, 12, 13]. The first approach is challenging due to the need to protect the laser from heat, vibration and harsh engine environment conditions. Furthermore, this approach is also costly since stationary natural gas engines can have up to 16 or 20 cylinders[31]. The second approach uses optical fibers to deliver pump light to passively Q-switched end pump lasers that are mounted on individual cylinders [32]. This approach also may suffer from the aforementioned environmental challenges. However, compared to the first approach it is more cost effective, due to the use of a single pump source multiplexed to different

laser systems on the engine cylinders. The third approach uses fiber lasers based on actively doped fiber material to create gain within the fiber itself. Such systems can be multiplexed; however, the current state of the fiber lasers does not support the power levels and energies needed for ignition in engines [33]. The fourth approach is promoted by our research group at Colorado State University and is viewed as the most-cost effective system[8, 12, 13]. In this approach, a remotely located single laser source is multiplexed to different engine cylinders via passive optical fibers, thus eliminating the need for multiple lasers and avoiding the problematic effects of harsh engine environments on optics.

The system architecture that our group is developing for the fourth approach consists of i) a laser source (likely a diode pumped solid state laser at 1064 nm), ii) a multiplexer (based on either a rotating galvo or electro-optic or acousto-optic modulators) to switch the beam to the fibers, iii) passive optical fibers(hollow core fibers, photonic crystal fibers or solid step index silica fibers) to deliver the laser beam from the multiplexer to the cylinders, iv) an optical spark plug on each cylinder consisting of a focusing lens and a window. Figure 1.7 shows an image of such a system as was used for demonstrating fiber delivered laser ignition system on a Caterpillar G3516C engine, as well as schematic diagram of an optical spark plug.

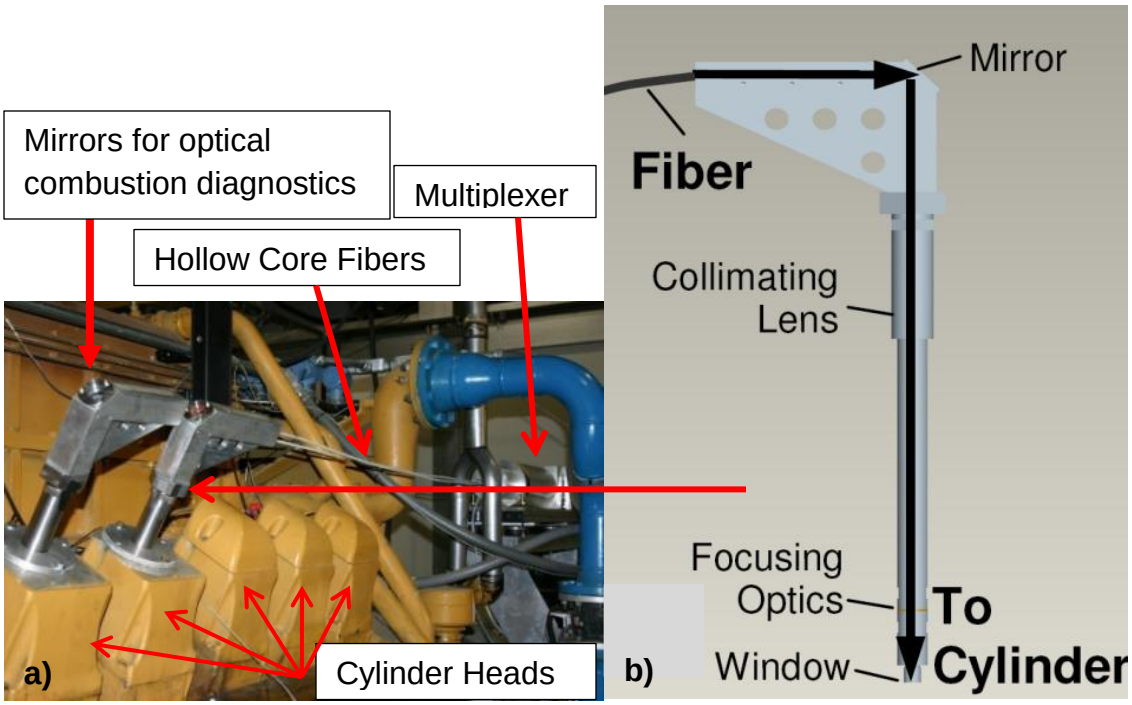

Figure 1.7:(a)Photograph of multiplexer, with the use of hollow core fibers, on a Caterpillar G3516C engine,and (b) schematic diagram of optical spark plug used in the engine testing.

1.2 Fiber Delivery of High Power Laser Pulses

Our research has been geared towards developing a laser ignition system based on multiplexed fiber delivery of laser pulses. Fiber delivery of laser pulses is especially challenging because of the need to deliver laser beam with enough spatial quality (M^2) to focus it into small spots with sufficient power to reach the breakdown threshold [13, 33, 34]. Figure 1.8 shows a schematic of a basic setup of fiber delivery for laser pulses and spark formation.

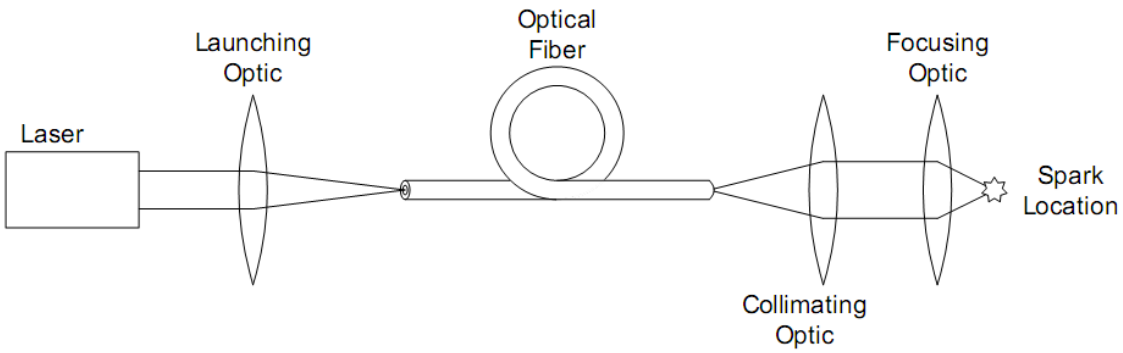

Figure 1.8: Setupfor fiber delivery of laser pulses and sparks formation.

As discussed before, intensity of ~200 – 300 GW/cm^2 is required to create sparks in atmosphere pressure air. (This breakdown threshold intensity is taken as the minimum intensity requirement that must be achieved in order to create a safe margin relative to the required intensity at higher motored pressures, which is lower). The spatial beam quality parameter (M^2) is a measure of spatial coherence and thus how tightly a laser beam can be focused. Figure 1.9 explains the concept of M^2 and associated focusing. It assumes that the beam out of the fiber is collimated (with a first lens) and focused (with a second lens) as shown in Fig. 1.8.Fig.1.9 and equations (1.1-1.4) allow calculation of beam spot sizes and intensities based on embedded Gaussian concepts [35]:

$$w_f = \frac{\lambda \times f \times M^2}{\pi \times w_l} \tag{1.1}$$

$$z_R = \frac{\pi \times w_f{}^2}{\lambda \times M^2} \tag{1.2}$$

$$w(z) = w_f \sqrt{1 + \left(\frac{z}{z_R} \right)^2} \tag{1.3}$$

$$I = \frac{E_p}{t_p \times \pi \times w(z)^2} \tag{1.4}$$

where w_f is the waist (radius) achieved with the real (M^2>1) beam, w_l is the radius of the launch beam on the focusing lens, $\lambda$is the wavelength of the laser, f is the focal length of the focusing lens, M^2 is the beam quality, z_R is the Rayleigh range (for which the beam radius is $\sqrt{2}$ w_f), $w(z)$ is the beam radius along the direction of laser propagation, z is the distance along the optical axis from the focal point, I is the average intensity (assuming the beam uniformly fills a circle defined by the radius), E_p is the pulse energy, and t_p is the pulse duration of the laser. The size of the launch beam (w_l) can be changed by appropriate selection of collimating lens. From these equations, for a fixed lens and incident beam diameter on the lens, one can see that higher M^2 beams result in larger focused spot sizes (w_f), longer Rayleigh range (z_r), larger radius ($w(z)$), and lower beam intensities (I).

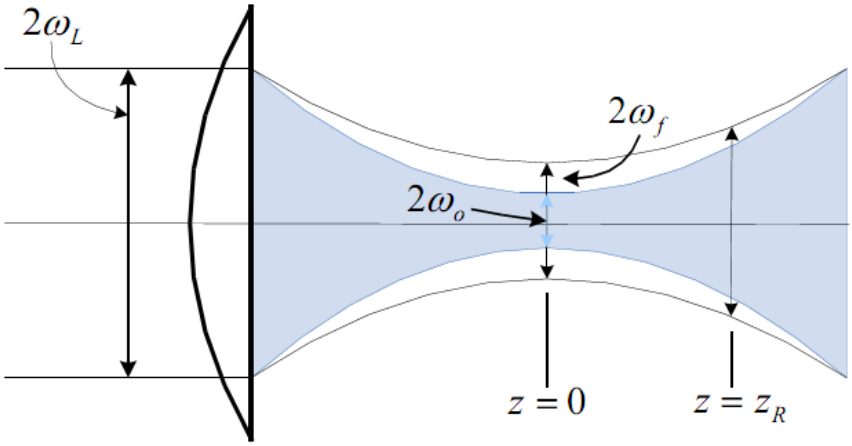

Figure 1.9: Focusing of an ideal Gaussian beam (M^2 = 1, shaded) and a real beam (M^2> 1). w_o is the waist (radius) achieved with ideal (M^2 =1) beam; w_f is the waist (radius) achieved with the real (M^2>1) beam.

Single mode fibers with small core diameters deliver laser beam with high beam quality (M^2 ~ 1) but cannot handle high peak powers [8]. On the other hand, multimode step-index silica fibers with relatively large core sizes can support delivery of multi-mJ pulses, but they also support multiple spatial modes (and hence high M^2) making it challenging for focusing [34]. Sparking and ignition have different requirements in terms of intensity and energy (Section 1.1.4), so that one can consider strategies to create sparks and then deposit additional energy. For example, fibers that support high quality beam propagation with just enough energy for sparking can be used. The energy in such sparks can be augmented with a second laser pulse that may come from fibers with larger cores but poorer beam quality. Such a dual pulse approach for ignition is described in Chapter 4.

Research at CSU has so far been focused on two key fiber candidates for delivering laser pulses – hollow core fibers and solid core step index fibers. These fibers are discussed in the following section.

1.2.1 Hollow Core Fibers

Yalin et al. first demonstrated the use of cyclic olefin polymer-coated (COP) hollow core fibers to deliver nanosecond laser pulses to form sparks in air [13]. A cross section of such a hollow core fiber is shown in Figure 1.10. They reported fiber output beam of 47 mJ pulse energy with M^2 of 11. The beam was focused to 24 µm to achieve intensity of ~300 GW/cm^2 to form sparks in atmospheric pressure air. However, the fibers showed poor performance (reduced transmission and high M^2) in coiled or bent configurations, making it challenging to use them on the engine. For example, when the fiber was bent to a radius of curvature of 1.37 cm, transmission dropped down to 66% and M^2 increased to 20. Nonetheless, a delivery configuration with 1mm inner core diameter hollow core fiber held in a straight configuration was used to deliver 1064 nm (Nd:YAG) laser pulses to operate a single cylinder of a Waukehsa VGF 18 engine, thereby providing the first demonstration of running an engine with fiber delivered laser ignition system [8]. The engine tests showed the highest peak pressure and the shortest ignition delay for the cylinder run with laser ignition system. Subsequent tests were conducted with hollow core fibers used to deliver laser pulses from a 1064 nm (Nd:YAG) laser to operate two cylinders of a Caterpillar G3516C engine using a multiplexer[12]. The tests showed 100%

ignition, albeit with lower indicated mean effective pressures (IMEPs) compared to the baseline results (that were obtained with the original electrical spark plug ignition system). Nonetheless, the results showed the ability of the fibers to spark and ignite the fuel air mixtures consistently. It was realized that the differences stemmed to the different optical plug configurations (See Chapter 2). Nonetheless, the inability of these fibers to deliver high quality beams in coiled configurations makes these fibers challenging for practical engine implementations.

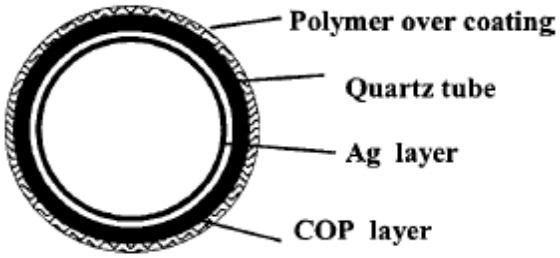

Figure 1.10: Schematic diagram of a hollow core fiber. COP refers to cyclic olefin polymer[13].

1.2.2 Solid Core Step Index Silica Fibers

In contrast to hollow core fibers, step index solid core silica fibers are widely understood in terms of performance, damage limits etc. However, large core step index silica fibers deliver highly multimode output (high M^2), which makes it challenging to focus the beam tight enough for breakdown. Very recently, Joshi et al. have investigated a novel approach using solid core step index fibers for delivery of high peak power pulses to form laser sparks[36]. The fibers used had 400 µm core diameter but with an unusually larger 720 µm cladding. More typical

fibers with a 400 µm core would have a thinner 440 µm cladding. The large cladding provides rigidity to the core-cladding interface thus reducing the micro-bends of the core-cladding interface and the mode coupling within the fiber. As a result, Joshi at al. obtained M^2 of 2.6 out of the2 m length 400 µm core fiber[36]. In contrast, a similar size core fiber but with thinner cladding would produce M^2 of ~40. Similarly, Hurand et al. [34] also showed that 200/330 and 200/745 µm fibers have M^2 of 11 and 2.8 respectively. (The notation 200/745 µm refer to a fiber of core size 200 µm and cladding size 745 µm.) Figure 1.11 show the spatial profile of the beam output from the 200 µm core fibers of different cladding thickness.

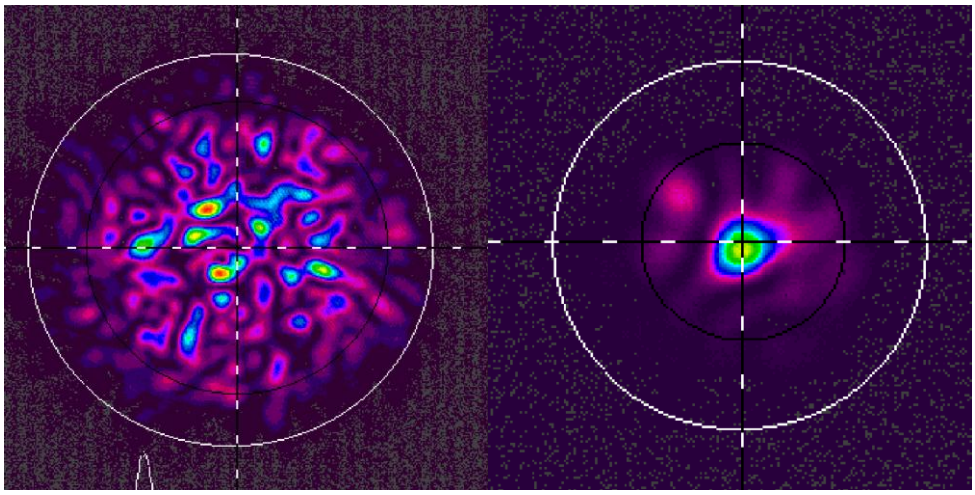

Figure 1.11: Output beam profiles for 200/330 µm fiber and 200/745 µm fiber with M^2 of 11 and 2.8 respectfully[34].

Joshi et al. [36] also showed spark delivery of 1064 nm light, via a 400/720 µm fiber with 3 - 4 mJ of pulse energy, 10ns pulse duration, and in atmospheric pressure conditions. However, as discussed earlier, these energies are below the 10-20 mJ pulse energies needed for ignition. Alternative techniques will be

required to achieve these energy levels, for example, use of pulses with higher energy and longer pulse duration (to keep the peak power constant), or dual pulse approaches where the first pulse forms a spark and the subsequent pulse deposits energy into the spark.

1.3 Problem Statement

The current research focuses on two main issues: i) investigate the reasons behind lower IMEPs obtained for laser ignited cylinders of CAT G3516C engine when operated with hollow core fibers, and ii) experimentally investigate the effect of using dual laser pulses to increase the total amount of energy deposited in a laser spark. Chapter 2 focuses on the first issue and examines different optical plug designs used during engine testing. These plugs included non-fueled electric prechamber plug, a non-fueled laser prechamber plug, and an open chamber laser plug. Chapter 3 focuses on the initial use of computational fluid dynamics (CFD) to model the fluid flow inside the prechamber plug and ascertain the impact on the ignition. Chapter 4 focuses on the second issue, i.e. the use of dual pulse approaches for laser ignition. Specifically, pulses with different pulse durations, beam profiles, energies, and varying inter-pulse delays are investigated to understand their effect on energy deposition into a pre-ionizing spark. Visualization techniques are used to measure the plasma sizes for single and dual laser pulses. The dual pulse energy addition approaches may also benefit LIBS diagnostics. The final chapter provides conclusions and recommendations for future work.

Chapter 2

OPENAND PRECHAMBER LASER IGNITION

All the published works on laser ignition of automotive (gasoline) and stationary natural gas engines have been with open chamber plugs, i.e., the laser beams are focused inside the open volume of the main combustion chamber by a lens to form a single combustion initiating spark (Fig. 2.1b). On the other hand, (non-laser) experiments have shown increase in fuel efficiency and reductions in emissions through the use of indirect (prechamber) electric spark ignition[37, 38]. A prechamber intensifies and accelerates the combustion in the main chamber by generating turbulent gas jets in the main combustion chamber. However, the choice of the optimum ignition approach, for example, fueled prechamber plug (in which a prechamber is equipped with a separate fuel supply system), non-fueled prechamber plug (where the fuel and air mixture is fed into the prechamber through the jet holes during the compression stroke), or conventional open chamber ignition is engine specific. The optimum ignition system for a given engine depends on factors including in-cylinder fluid mechanics, engine heat transfer, and in-cylinder mixing each of which also influences engine efficiency and emissions.

Furthermore, the ignition (sparking) location also needs to be optimized by taking into account the degree of local turbulence and flow velocity that can impact the initial flame kernel development and flame propagation. For example, swirl generating orifices entering the prechamber lead to high flow velocities and turbulence intensities in the center of the prechamber as compared to the base[39, 40]. In the case of unscavenged prechambers, the fuel-air ratio distribution is also not homogenous inside the prechamber and is generally leaner in the center than at the base of the prechamber [41].

In this work, engine testing of a Caterpillar G3516C engine with three types of ignition configuration is reported: a) non-fueled electric prechamber plug with electrodes at the base of the prechamber, b) non-fueled laser prechamber plug with laser spark in the middle of the prechamber, and c) open chamber plug with laser spark in the main chamber. The overall goal of the research is to compare and understand the performance of the three different ignition methods in the engine. Chapter 3 presents CFD modeling of the prechamber and therefore also contributes to examining these combustion methods.

The layout of this chapter is as follows. In Section 2.1, the experimental setup and the associated hardware developed for the engine testing are discussed. In Section 2.2, the results from the engine testing are presented and discussed.

2.1 Experimental Setup and Test Procedure

A single cylinder (#10) of a V16-Caterpillar G3516C engine was used to perform the comparative testing of the different ignition methods. The 4–stroke 16 cylinder turbo-charged natural gas engine is located at Engines and Energy Conversion Laboratory of Colorado State University and has a mechanical power rating of 1723 bkW at 1800 rpm. The engine uses a concentric bowl-in-piston design and has a compression ratio of 11.3. The bore diameter, stroke length, and total engine displacement are 170 mm, 190 mm and 0.069 m^3 respectively. The engine was loaded with a 1791 kW eddy current dynamometer and controlled using an in-house Labview program. The test cylinder was fitted with a pressure transducer (Kistler model 6125) and pressure data was acquired with a high speed data acquisition system (Hi-Techniques^{TM}). A 5 gas analyzer (Rosemount) was used to measure the exhaust concentrations of carbon monoxide (CO), total hydrocarbons (THC), nitrogen oxides (NO_x), oxygen (O_2), and carbon dioxide (CO_2) at both the cylinder exhaust port (by replacing the cylinder exhaust temperature sensor with an emission probe) and at the main exhaust port. The methane concentration in the fuel was also monitored to ensure consistency between different ignition tests and was found to be similar (6% by volume).

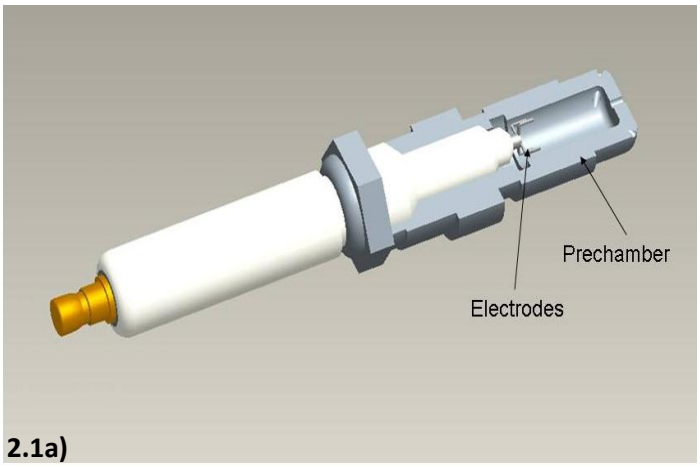

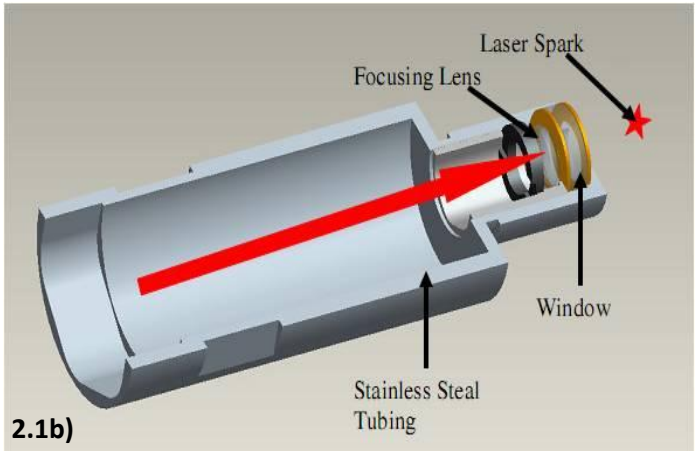

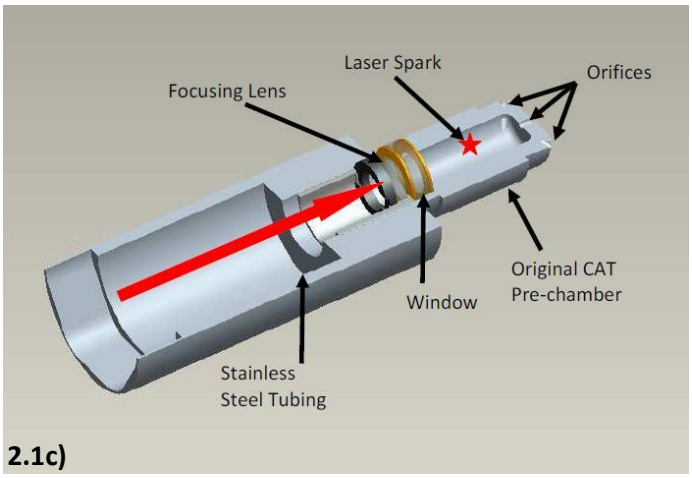

Figure 2.1: Cross sectional views of the different ignition plugs: a) non-fueled Caterpillar prechamber plug, b) open chamber laser plug, and c) non-fueled laser prechamber plug. The arrow and star indicates the laser beam path and the spark location respectively.

Figure 2.1 shows the cross section of the three types of ignition configurations used in the experiment: a) a non-fueled Caterpillar electric prechamber plug (EPP), b) a laser open chamber plug (LOP), and c) a non-fueled laser prechamber plug (LPP). The engine has coolant passages in the cylinder head around the spark plug port to cool the prechamber. The prechamber plug has a central electrode with four radially protruding electrodes and the electric spark is formed in the gap between the electrode and the ground prechamber body. Note that the spark is formed only in one gap at a time and may move from one gap to another gap in another cycle depending on which gap offers the least resistance.

A 1064 nm Q-switched (Nd:YAG) laser (CFR - Big Sky) with beam quality $M^2 < 2$ and 10 ns pulse duration was used for the laser ignition. Figure 2.2 shows the laser mounted on the laser plug assembly. The laser plug assembly consists of an aluminum head with a dichroic mirror, stainless steel tube and either LPP or LOP screwed onto the threads at the end of the tube. The dichroic mirror directs the laser beam onto the laser plug (LOP or LPP).The mounting configuration is selected to allow ready coupling of the laser beam to the laser plug given the layout of the valve head cover and casing above the cylinder.

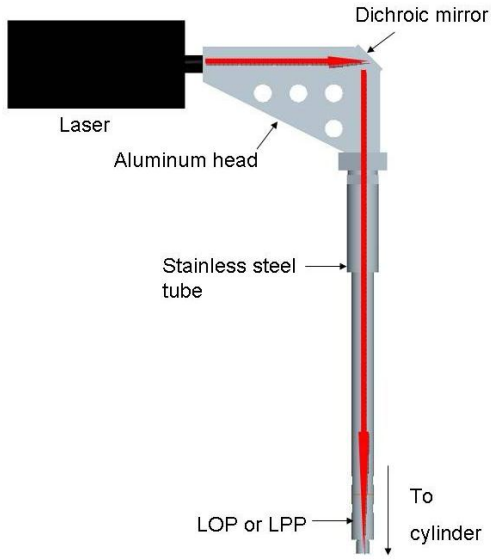

Figure 2.2: Laser and the laser plug (LOP or LPP) mounting assembly. The arrow indicates the laser beam path.

As shown in Fig. 2.1b, the open chamber laser plug consists of a 9 mm diameter focusing lens (with a focal length of 9 mm) and a sapphire window between two copper O rings. The laser beam is focused by the lens through the window and into the main combustion chamber. The laser prechamber plug in Fig. 2.1c is made by welding an original Caterpillar prechamber (from a Caterpillar spark plug as in Fig. 2a) onto a stainless steel tube. The tube holds a 9 mm focal length lens and a sapphire window. This design ensured that the prechamber laser plug was similar to the stock prechamber in terms of prechamber volume, number of jet holes (orifices), their sizes, and angles. The laser spark was formed at the center of the prechamber volume, which was 0.26%of the total clearance volume of the cylinder. The specifications of the prechamber are given in Table 2.1. The prechamber volume of the LPP design

was 18% lower than the prechamber volume of the EPP. This was due to the constraints in the retrofit design.

The laser energy delivered to the spark was held constant at 34 mJ. At these energy levels (and with 9mm focal length lens), the achieved focal intensities were ~1,000 GW/cm^2 which are far in excess of the ~200-300 GW/cm^2 needed for air breakdown at atmospheric pressure [20, 22, 42]. The laser was controlled by a pulse delay generator which was triggered by a pickup voltage from an inductive sensor placed on the spark plug wire of cylinder #4. The delay was set so that the laser was fired at a baseline ignition time of 24 degrees before top dead center (BTDC). This timing was selected for optimum performance at 1800 rpm and with the use of electrical prechamber spark plugs.

Table 2.1: Specifications of the prechamber laser plug.

Orifice Diameter	1.52	mm
Orifice Area	1.82	mm^2
Total Number of Orifices	5	
Orifice Angle	59.5^o and 27.1^o	
Prechamber Diameter	8.9	mm
Prechamber Volume	1090	mm^3
Prechamber Volume to Total Clearance Volume	0.26	%

The three ignition approaches were compared based on the performance of the cylinder (# 10) at three different loads of 50%, 75% and 90% all at engine speed of 1800 rpm. The engine was run by setting the fuel-air ratio for 1 g/hp-hr NO_x output at the main engine exhaust port; however, precise control of in-cylinder air-fuel ratio from one test to another was difficult in this engine test setup. The measured exhaust O_2 (%) at the cylinder exhaust port and inlet air relative humidity (RH %) for each test condition are given in Table 2.2. The baseline engine testing with EPP was done on a day prior to the tests with LOP and LPP. At each load, 1000 pressure cycles were recorded and the exhaust emission was sampled for 5 minutes. In-house data analysis software was used to analyze test data obtained from in-cylinder pressure measurements.

2.2 Engine Test Results and Discussion

The engine (cylinder #10) performance data for the laser prechamber plug and the laser open plug with the electric prechamber plug are compared in Fig. 2.3 and Fig. 2.4. Uncertainty bars for average IMEP and peak pressure location was determined by standard error with a sample size of 1,000.

Table 2.2: Test conditions for EPP, LOP, and LPP tests.

Load (%)	**50**			**75**			**90**		
Ignition Method	**EPP**	**LOP**	**LPP**	**EPP**	**LOP**	**LPP**	**EPP**	**LOP**	**LPP**
Average exhaust O_2 (%)	9.25	9.25	9.30	9.55	9.58	9.52	9.69	9.78	9.60
Inlet Air Relative Humidity (%)	36.2	23.1	25.4	31.9	22.8	24.9	31.3	22.1	23.9
Methane (%)	87.6	85.5	85.0	87.5	86.4	86.2	87.5	85.8	86.5

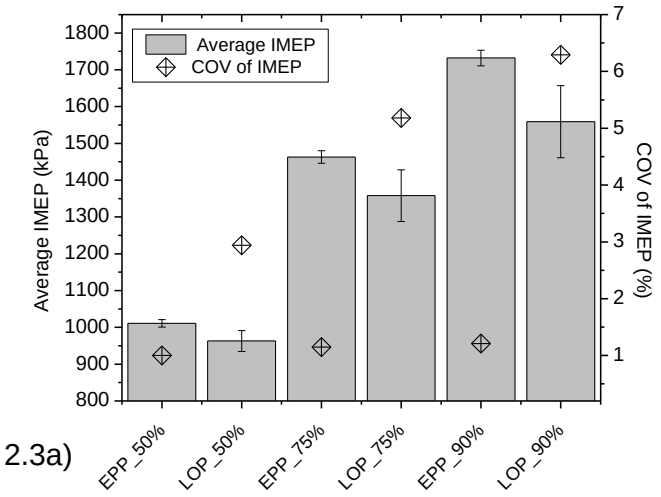

2.3a)

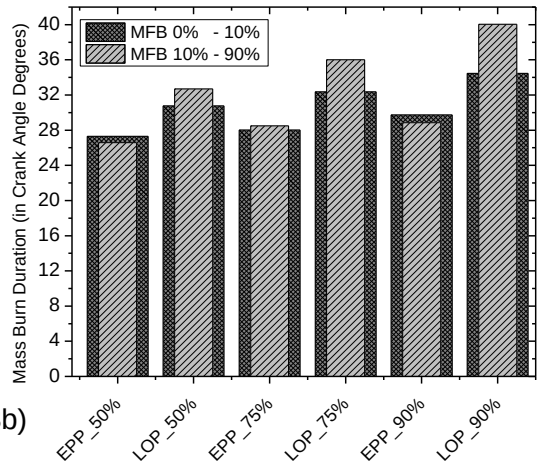

2.3b)

Figure 2.3: Comparison of EPP and LOP performance at 50%, 75% and 90% load; a) average IMEP and COV of IMEP, and b) 0 – 10% and 10% - 90% mass burn duration. Uncertainty bars for average IMEP are also shown.

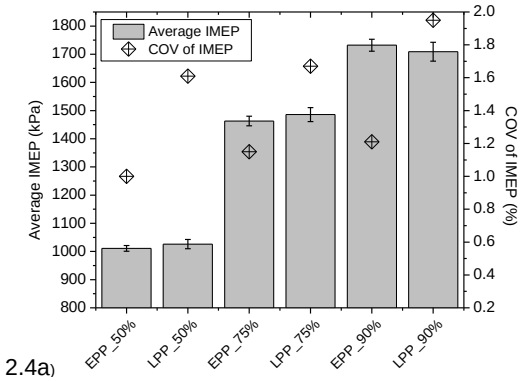

2.4a)

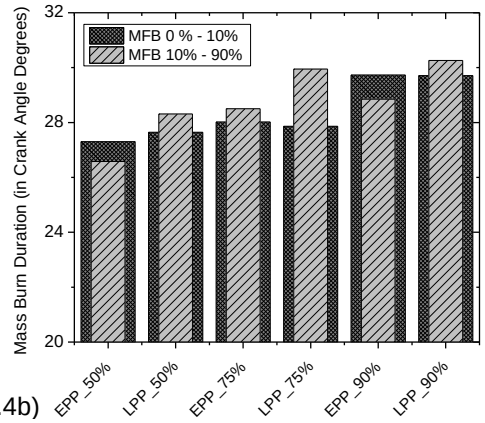

2.4b)

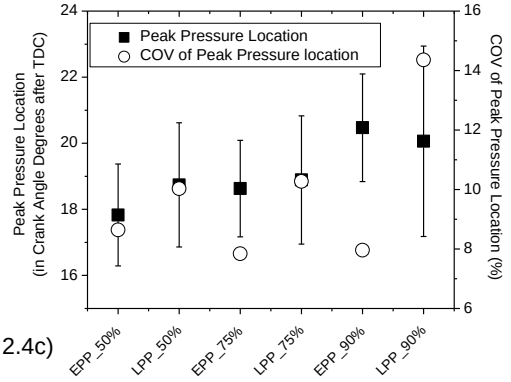

2.4c)

Figure 2.4: Comparison of EPP and LPP performance at 50%, 75% and 90% load: a) average IMEP and coefficient of variation (COV) of IMEP, b) 0–10% and 10-90% mass burn duration, and c) peak pressure location and COV of peak pressure location. Uncertainty bars for average IMEP and peak pressure location are also shown.

Reliable (100%) ignition and sparking was observed for all test conditions (i.e., for recorded 1000 pressure cycles). The ignition criterion was established by setting a threshold pressure at 32 degrees after top dead center and monitoring the number of pressure cycles whose pressure fell above this threshold. The significant test results from Fig. 2.3 and Fig. 2.4 are summarized as following:

i) The performance of LOP in terms of average indicated mean effective pressure (IMEP), coefficient of variation (COV) of IMEP and 0-10% and 10%-90% mass fraction burn durations at all load conditions is poorer compared to EPP. Although ignition was 100%, the cylinder pressure traces were erratic (with frequent spikes in THC emission at the exhaust) suggesting partial combustion and extremely poor combustion stability. Reasons for this are presented below.

ii) LPP and EPP show comparable average IMEP. However, the test data show higher variability in cylinder performance with LPP than EPP. For instance at 90% load, COV of IMEP is 1.9% compared to 1.2% for EPP, though both are below the allowed manufacturer's limits of 2% [43]. Although the average mass fraction burn duration 0-10% are comparable for the two cases, the 10-90% mass burn duration is slightly longer with LPP. As shown in Fig. 2.4c, the COV of peak pressure location for LPP is higher than with EPP. The higher variability in the peak pressure location suggests higher variability in the peak pressure and hence IMEP (which is observed in this case).

iii) The cylinder performance for LPP at 26 mJ was tested and there were no significant change in the cylinder performance.

The poorer performance of LOP compared to EPP can be explained by considering the nature of the engine and its associated fluid mechanics. The Caterpillar G3516C uses quiescent combustion chamber so as to minimize in-cylinder turbulence resulting in lower heat transfer to the cylinder wall and increased efficiency. The turbulence needed for the fast flame propagation in the main chamber is achieved with the multiple turbulent flame jets from the EPP. However, in the case of LOP, the combustion of the cylinder main charge is the result of a growing spherical flame from a single point spark source; hence, the combustion is essentially slower with LOP than when ignited with an EPP. Also, the peak cylinder pressure depends on the competing effects between heat release and increasing cylinder volume (during the expansion process). Cylinder peak pressures occurs a few crank angle degrees after the 50% of the cylinder charge (mass) is burnt. Therefore, the faster 50% mass is burnt, the higher is the peak cylinder pressure. The observed poorer performance of LOP is the result of the longer duration to burn 50% (and 90%) of the cylinder charge. These test showed that the observed lower IMEPs in past engine tests, with hollow core fibers and open-chamber plugs, were due to the type of ignition plug used.

In general, LPP showed comparable performance to EPP. As in the case of EPP, LPP ignites the charge in the main combustion chamber with the flame jets from the prechamber jet holes. Hence, the 0-10% and 10%-90% mass burn

durations are much shorter than in the case of LOP. Although the cylinder performance with LPP and EPP are comparable, the higher COV of IMEP and peak pressure location, and longer 10%-90% burn duration of the LPP suggest inconsistency in the intensity of the flame jets (i.e., jet penetration depth, temperature, and mass of the burnt gas) pushed out from the prechamber orifices (jet holes). The prechamber volume of the LPP is also 18% lower than the EPP possibly resulting in the observed combustion variability.

Furthermore, the observed higher combustion variations with LPP may be related to the combustion process inside the LPP itself. The flame speed and the consumption of the charge in the prechamber depend on the local flow velocity and turbulence [14]. However, the flow conditions at the locations where electric spark and the laser spark are formed within the prechamber may differ. The electric sparks are placed in a location where the local turbulence and flow velocities are not high enough to negatively impact the spark and the early flame kernel development [39]. In EPP, this is achieved by forming the electric sparks at the base of the prechamber where the spark and early flame kernel are shielded from the relatively high flow velocity and turbulence in the rest of the prechamber. In contrast, in the initial LPP design, the laser spark is formed at the middle of the prechamber where higher turbulence intensity and local flow velocity are expected [40].

Roethlisberger *et al*. have performed computational fluid dynamics (CFD) modeling of the flow field inside an unscavenged non-fueled prechamber for different prechamber designs[40]. In one of the simulations and for a prechamber

volume of 3000 mm^3, they found turbulent kinetic energy 70 times larger at the center of the prechamber than at the base of the prechamber. This finding is in qualitative agreement with the explanations discussed above. Chapter 3 presentsa CFD model designed for the prechamber optical spark plug used in this chapter (volume of 1086 mm^3).

In all the test cases, 100% ignition was observed showing the ability of laser sparks (and subsequent initial flame kernel) to withstand high turbulence and flame stretch. Additionally, these prechambers are not scavenged and the fresh fuel air mixture inside the prechamber is mixed with the residual burnt gas which can result in inhomogeneous fuel air ratio distribution within the prechamber. Furthermore, higher turbulence intensity and lean fuel-air conditions (inside the prechamber) lead to much higher ignition energy requirements than in quiescent mixtures[39, 44]. For example, using a high power pulsed electric spark ignition system, Huang *et al*. showed minimum ignition energy requirement of 2 - 3 mJ for igniting methane air mixture at equivalence ratio of 0.6 and laminar conditions[44]. However, at similar equivalence ratio, they found the minimum ignition energies to increase from 2.14 mJ to 70 mJ depending on the level of turbulence. Due to limited laser energies available in this experiment, the effects of higher laser energy on the associated combustion variabilities could not be tested.

Chapter 3

CFD MODELING OF FLOW IN PRECHAMBER

Computational fluid dynamics (CFD) has been extensively used to model flows and combustion in internal combustion engines [40, 45-47]. Roethlisberger et al. [40] have used CFD modeling to understand and optimize the shape and size of prechamber electrical ignition system. Similarly, Dors et al. [46] used CFD to model the laser spark evolution for a 10 ns laser pulse.

As was also mentioned, there is a need to understand the flow field inside the optical prechamber used in the engine studies (Chapter 2). This chapter will investigate the flow field (with no spark or combustion) with CFD. Three possible spark locations are selected and analyzed for velocity magnitude (v) and turbulence kinetic energy (k) (equations are shown below). Optimizing the spark location is important because if the spark location has high turbulence then it will take more energy to ignite the mixture. In turn, this may lead to premature optical damage of the fibers as well as the need for higher power (more expensive) laser sources. The flow fields are analyzed for in-cylinder pressures corresponding to two loads (50 and 90%) of the Caterpillar G3516C natural gas engine running at 1800rpm. The model used was Renormalization group (RNG) k-epsilon turbulence sub-model. This turbulence sub-model was selected due to its ability to calculate smaller scale motion by renormalizing the Navier-Stokes

equations (k-epsilon model) as shown by Yakhot et al.[48]. Meshing is done in Gambit while the modeling is done in Fluent 12. A user defined function (UDF) has been written to simulate the in-cylinder pressures.

The following equations are used to find instantaneous (time dependent) turbulent kinetic energy, k(t) and velocity magnitude, v [49]:

$$k(t) = K + k \tag{3.1}$$

$$K = \frac{1}{2}({V_x}^2 + {V_y}^2 + {V_z}^2) \tag{3.2}$$

$$k = \frac{1}{2}(\overline{{\acute{v}_x}^2} + \overline{{\acute{v}_y}^2} + \overline{{\acute{v}_z}^2}) \tag{3.3}$$

$$v = \sqrt{{V_x}^2 + {V_y}^2 + {V_z}^2} \tag{3.4}$$

where, K is the mean kinetic energy, k is the turbulent kinetic energy, V_z, V_y, $V_z$are the mean velocities, and $\acute{v}_x$, $\acute{v}_y$, $\acute{v}_z$are the time varying fluctuating velocities for the x-component, y-component, and z-component respectively.

3.2 Volume Meshing

The optical spark plug was modeled in Pro-Engineer modeling software as shown in Figure 3.1, and then imported into gambit. The optical prechamber volume was split into two sections which in turn were meshed in two different ways as shown in Figure 3.2. Part A, which includes the inlets, was meshed with a Tet/Hybrid with a scaling factor of 1.25. This allowed a fine mesh at the inlets to replace boundary layering. No boundary layer meshing was used due to the difficulties posed by the odd angles caused by the inlets. Part B, the bottom of the prechamber, was meshed with Hex/Wedge to equally divide the cylinder

base of the prechamber. The entire volume encompassed 29,013 cells with maximum cell squish and skewness of 0.78 and 0.96 respectively.

The boundary conditions used at the inlet surfaces of the five ports (on the top of the prechamber) are pressure inlets, whereas all other surfaces are walls. The pressure inlet boundary condition was used due to the fact that there are no pressure, or velocity, outlets present and compressible flow was used.

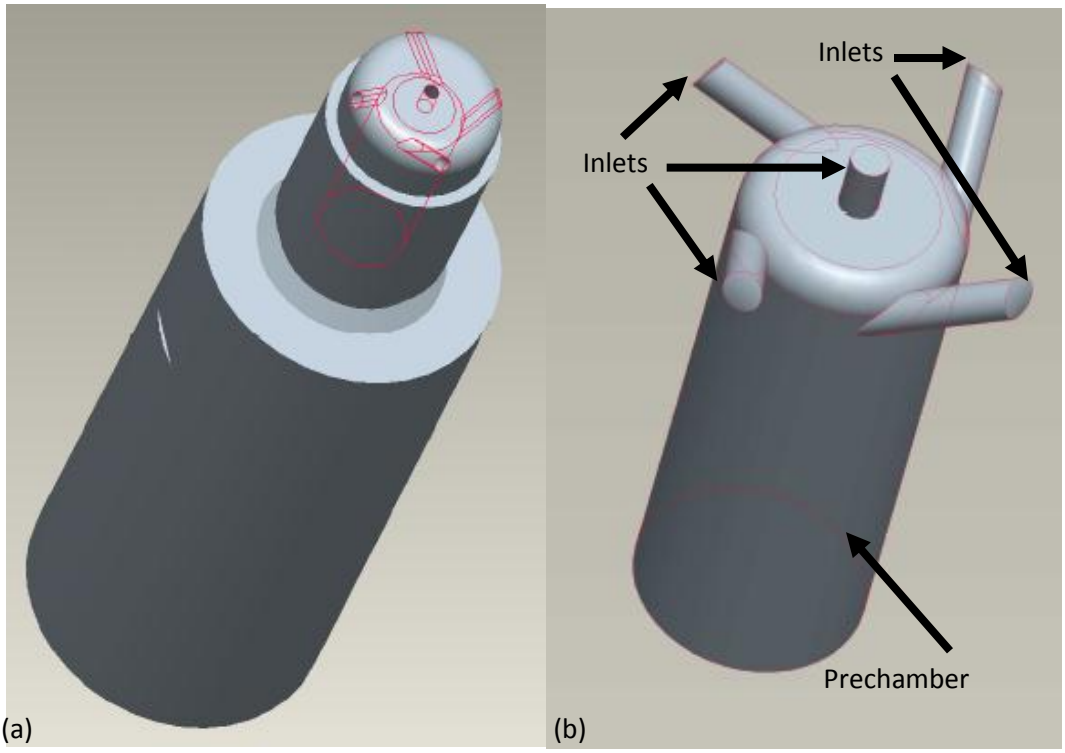

Figure 3.1: Pro E drawings of (a) optical spark plug and (b) prechamber with inlets only.

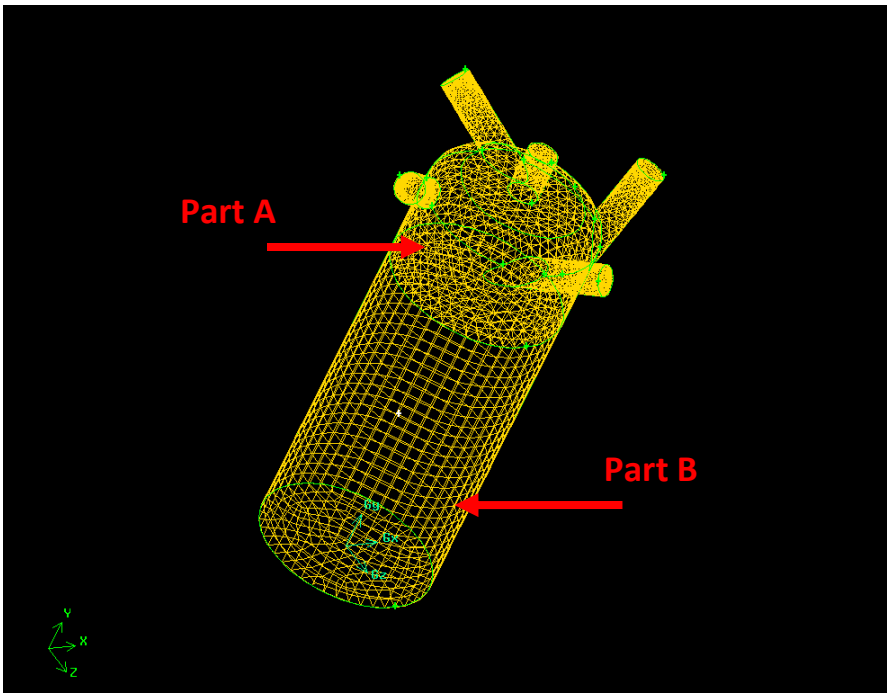

Figure 3.2: Mesh of prechamber optical spark plug created in Gambit. Part A has a Tet/Hybrid mesh with a scale factor of 1.25. Part B has a Hex/Wedge mesh with no scale factor.

3.3 Fluent

The completed mesh was imported into Fluent 12. The working fluid used in the modeling was just air, although fuel and air mixture is also possible but is not used in this initial simulation. Because we are interested in lean mixtures (>94% air by volume), this approximation is considered reasonable. The main goal of this work is to model the flow inside the prechamber up to ignition time (although the fluid motion after the ignition would also be interesting from the point of flame development).The modeling was done in transient time with a density based solver. (Transient time was used to simulate the time dependent flow into the prechamber. Density based solver was used due to the use of pressure inlet boundary conditions on the five port inlet surfaces.) For the pressure inlets, the

turbulent kinetic energy (k_{S_P}) and turbulent dissipation rate (ϵ) were set to 65.3 $m^2/s^2$and 81,200 m^2/s^2respectivelyas found from the following equations: [40]

$$k_{S_P} = 0.5S_P^2, \tag{3.5}$$

$$\epsilon = C_\mu^{3/4} \frac{k_{S_P}^{3/2}}{\ell}, \tag{3.6}$$

$$\ell = 0.07 d_h \tag{3.7}$$

where$C_\mu$is the turbulence model constant($C_\mu = 0.09$), S_P is the mean piston speed (S_P = 11.4 m/s), l is the turbulent length scale, and d_h is the hydraulic diameter (d_h = 1.5 mm).The temperature entering the prechamber was assumed constant (800 K). The initial conditions for velocity (in all directions) was set to 0 m/s and total pressure were set to 300 kPa gage (for 90% load) and 250 kPa gage (for 50% load). The flow inside the prechamber, when the piston is near bottom dead center (BDC), is assumed to have no dominant direction. The renormalizing group (RNG) k-epsilon viscous model was used for both loads.

A critical aspect of the simulation is proper selection of the time step size used when running the simulation. This is partly due to the pressure curve used in the user defined function (UDF) (see section 3.3.1).When the time step was too large, the pressure differential between the inlet plane and the next plane (volume) became too large, so as to produce a non-physical shock wave (shown in Figure 3.3). Therefore the time step was reduced until flow contained no shock waves.

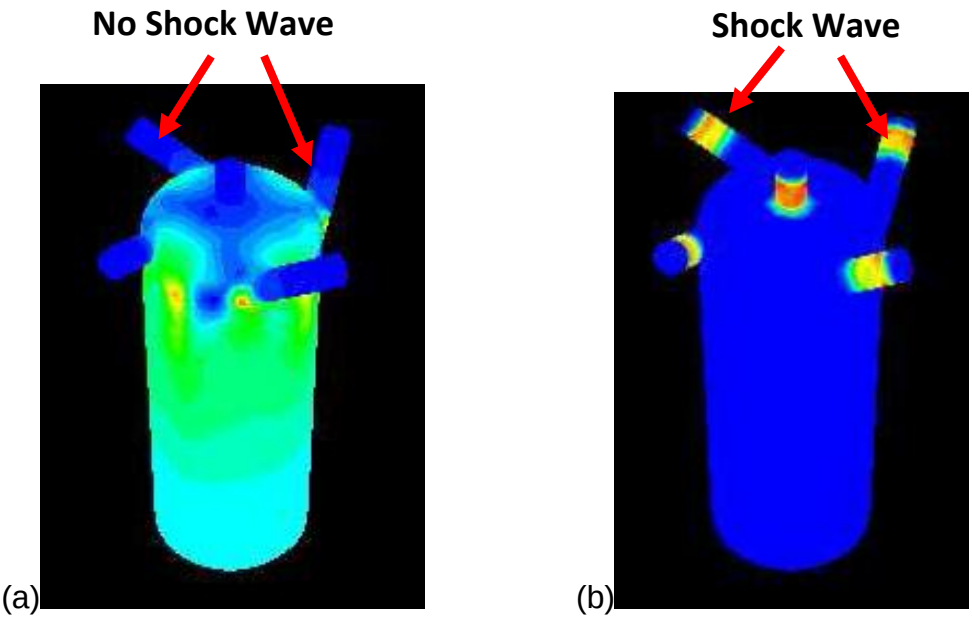

Figure 3.3: Static Pressure filled Contours images with both 0.00001 sec (a) and 0.0001 sec (b) time steps

3.3.1 User Defined Function

A user defined function (UDF) is a tool used in computational fluid dynamics programs to simulate a pressure or flow velocity at pressure or velocity inlets verses (transient) time. In the case of the optical prechamber analysis, a UDF was used on all five pressure inputs to the prechamber. An example of the UDF used in the model is shown in Figure 3.4. Use of the UDF provided a way to simulate the effect of the compressing piston motion and therefore reduced the number of cells needed to model the prechamber flow (as opposed to also explicitly modeling the cylinder and piston). This in turn reduced the run time and complexity of the mesh. The pressure curves were taken from a Caterpillar G3516C natural gas stationary engine, running at 1800 rpm with 50 and 90% loads, and then fitted with a fourth order polynomial. To keep the computation

time even lower, the pressure curve used in the modeling was truncated between the start of the cylinder pressure increase and 10 crank angles past the point of ignition as shown in Figure 3.5. One (single user) personal computer was used to run model with approximately three days of run time.

```
/*Fluent 12
/*User-Defined Function:
/*90% Load
#include "udf.h"
DEFINE_PROFILE(inlet_pressure, thread, position)
{
float pressure, t, pressure2;
double power2, power3, power4;
face_t f;
  t = RP_Get_Real("flow-time");
  power2 = pow(t, 2);
  power3 = pow(t, 3);
  power4 = pow(t, 4);
  pressure2 = 8.4446e11*power4 - 1.1794e10*power3 + 6.4345e7*power2
-9.0014e4*t + 3.4837e2;
pressure = pressure2*1000;
begin_f_loop(f, thread)
  {
   F_PROFILE(f, thread, position) = pressure;
  }
end_f_loop(f, thread)
}
```

Figure 3.4: User defined function (UDF) at 90% used to simulate pressures at the inlet.

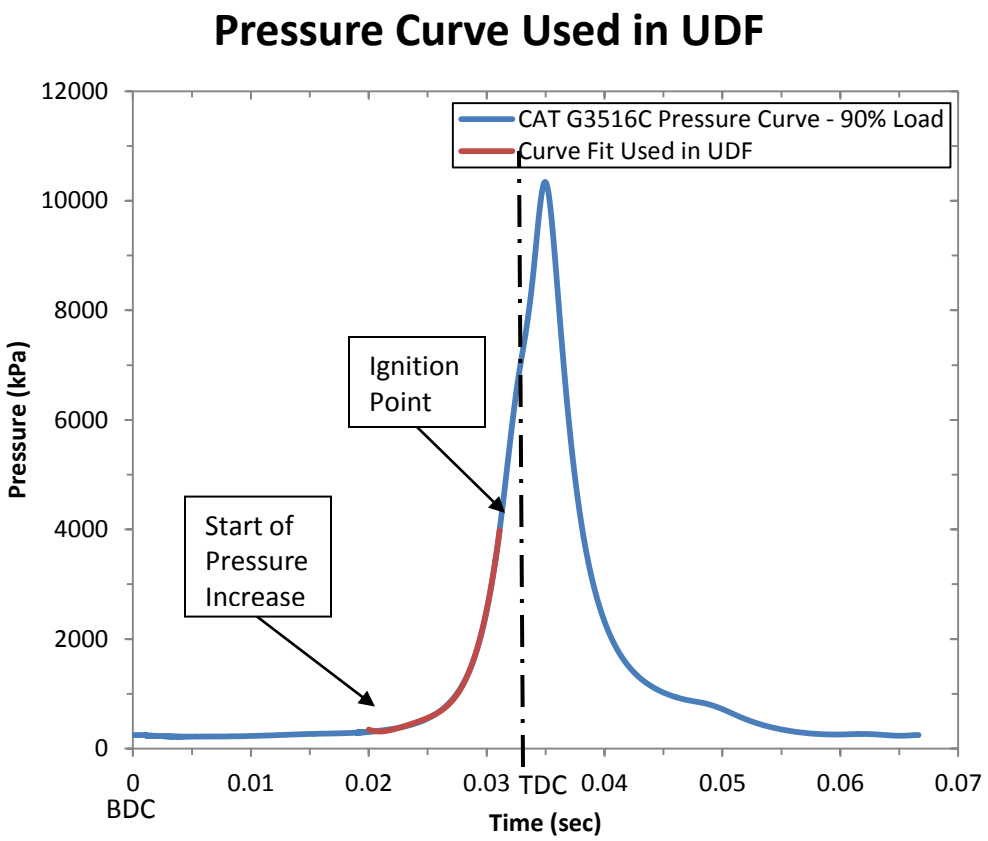

Figure 3.5: Pressure curve used in the user defined function (UDF) for all five pressure inlets.Note: Bottom dead center (BDC) and top dead center (TDC) are indicated.

3.4 Modeling Results and Discussion

For each modeling case, the flow was analyzed at four locations within the prechamber. Figure 3.6 shows a 2-D plane view (cut-away)of the prechamber. Four analysis points within the plane were selected as shown in Fig. 3.6. Point 1 is quarter way up from the bottom, point 2 is in the middle, point 3 is 2 mm from the top of the prechamber, whereas the fourth point is in the middle of one of the side inlets. The first three points are located on the center axis of the prechamber and represent possible spark locations (during the engine tests, the

spark was located in the middle of the prechamber at point 2). The point inside the inlet is used to understand the flow into the prechamber.

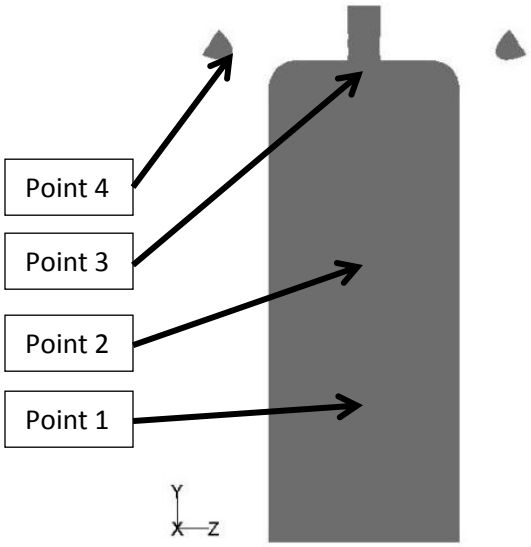

Figure 3.6: A cut-away section/plane of the prechamber showing the 4 analysis points.

Figures 3.8 and 3.9 show contours velocity magnitude (v) and turbulent kinetic energy (k). Figures 3.10 and 3.11 show the turbulent kinetic energy and velocity magnitude for the four points, 1-4.Figures 3.8 and 3.9 show little visual difference between both loads for both sets of images, this could be due to similar pressure curves used in the UDF as shown in Figure 3.7. They also show asymmetric behavior that could be caused by the use of transient flow and the development of unsteady flow. Since this model is performed on the full geometry of the prechamber the four side inlets should form symmetric turbulent flow, and since the images are showing asymmetric flow it is most likely caused by the top inlet entering the prechamber (further research is required).At point 3, located 2mm from the top of the prechamber, both v and k are similar to the

corresponding inlet values (point 4) with slight reduction of approximately 12% and 15% respectively. As the spark location gets further away from the top of the prechamber there is a larger drop in both velocity magnitude and turbulent kinetic energy. At point 2, located in the middle of the prechamber, there is approximately a 38% and 55% drop in velocity magnitude and turbulent kinetic energy respectively. At point 1, v and k further reduced to approximately 5 m/s and 2 m^2/s^2. Of the 4 analysis points, point 1 has the lowest velocity and turbulent kinetic energy making it a favorable spark location (as it would yield the least flame stretching and quenching). However, as mention earlier, only air has been used as the fluid and the current modeling does not consider fuel-air distribution within the prechamber. Hence, at point1, although fluid conditions might be favorable, it may not have the needed fuel air distribution. A CFD simulation with fuel air distribution will give the complete picture of the optimum spark location. The inlet turbulent kinetic energy, point 1, is showing very low turbulent kinetic energy due to the levels of laminar flow (resulting from the UFD). Roethlisberger et al. showed that when modeling both main chamber and prechamber the turbulent flow developed in the main chamber is shown to enter the prechamber [40].

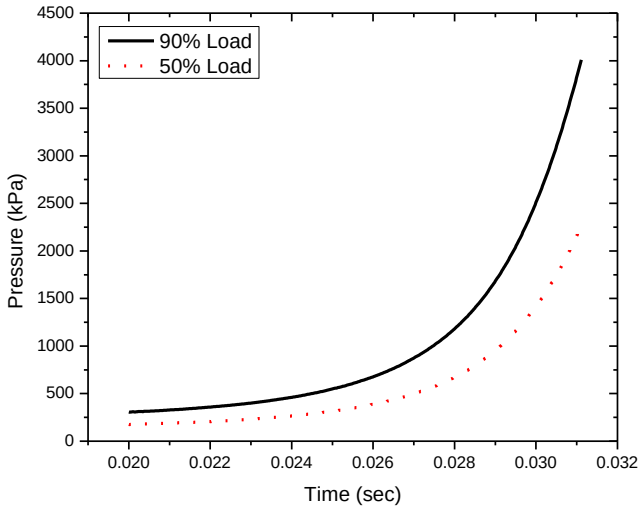

Figure 3.7: Motored pressure (UDF) curves for 50% and 90% loads.

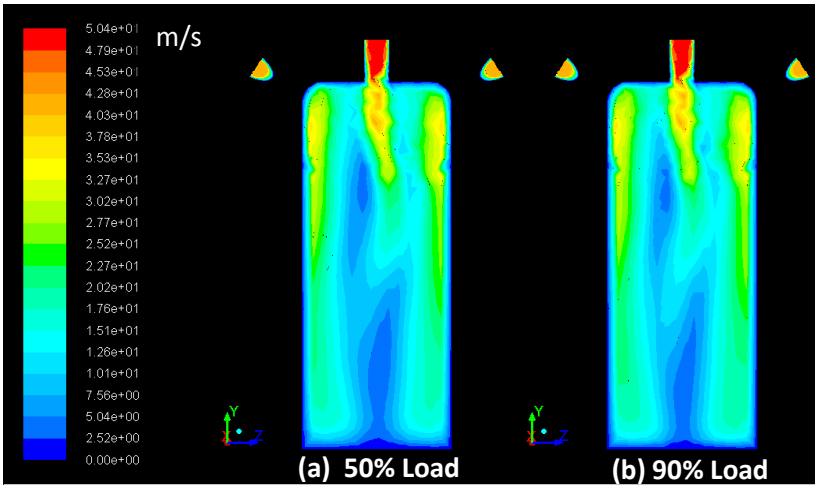

Figure 3.8: Contours of velocity magnitude at 24 degrees BTDC (point of ignition) for both loads: (a) 50% and (b) 90%.

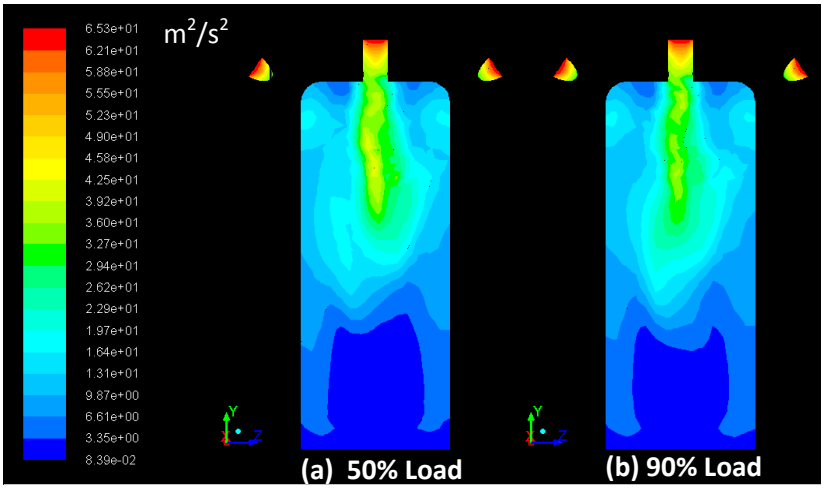

Figure 3.9: Contours of turbulent kinetic energy (k) at 24 degrees BTDC (point of ignition) for both loads: (a) 50% and (b) 90%.

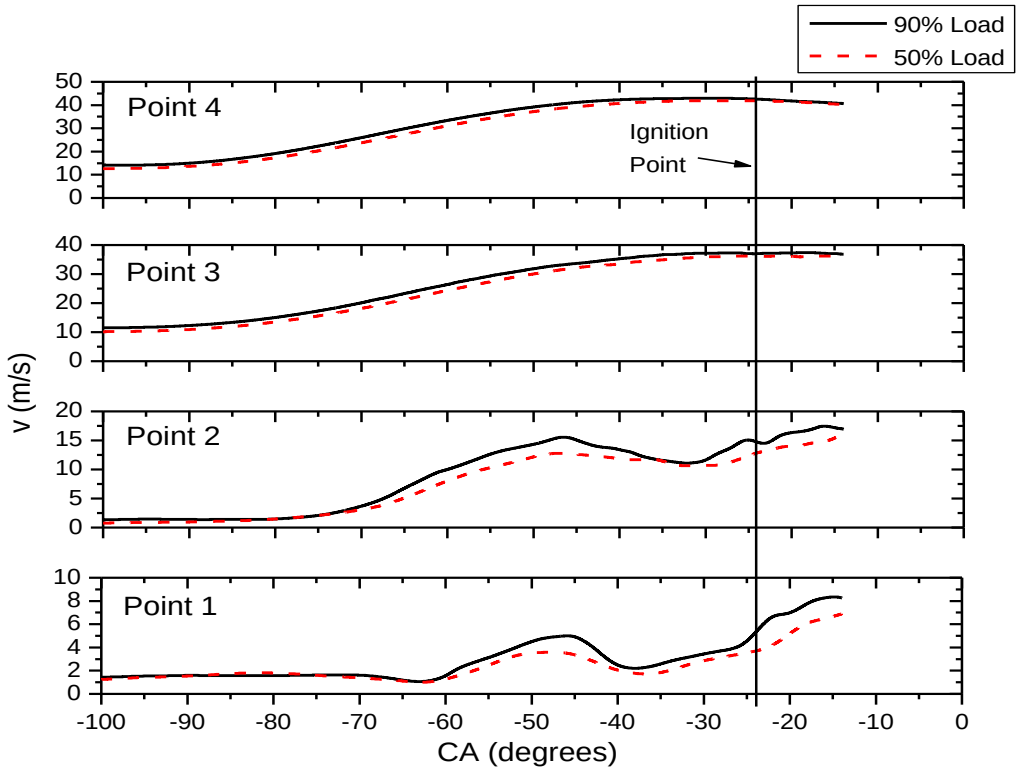

Figure 3.10: Velocity magnitude versus crank angle at the four analysis points (see Fig. 3.6).

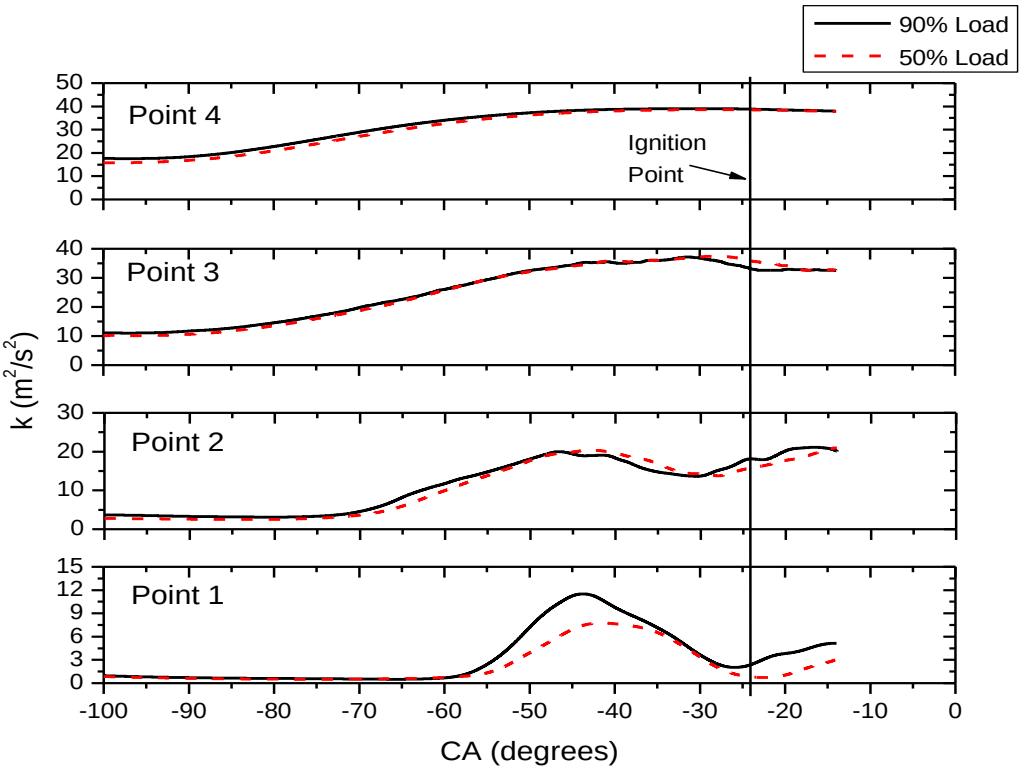

Figure 3.11: Turbulent kinetic energy (k) versus crank angle at the four analysis points (see Fig. 3.6).

Chapter 4

DUAL PULSE APPROACH TO LASER IGNITION

This chapter presents experimental results on new approaches employing pre-ionizing pulses to enhance and control laser plasma formation in gases. Such strategies allow for tailoring the two pulses (for example, wavelengths, pulse durations, energy content, inter-pulse separation) in order to obtain laser sparks with sufficient energy for the needed application. Despite a large body of research in laser breakdown using single laser pulses there has been very minimal research on multi-pulse approaches and pre-ionization. Our initial results shows the potential of multi-pulse approaches based on use of an initial pulse to achieve pre-ionization with a second pulse for generation of additional ionization (i.e. electron avalanche ionization (EAI)) and energy addition. Such laser plasmas may ultimately allow improved combustion performance in a wide range of ignition applications as well as new light sources for laser induced breakdown spectroscopy (LIBS) diagnostics.

The basic principle of double pulse is shown in Figure 4.1. The first pulse pre-ionizes the air (in the case of nanosecond pulse duration a spark is formed). After some time a second pulse is introduced to add energy to the preformed plasma. The first and second pulses are called the pre-ionization leg (PL) and energy addition leg (EAL) respectively. The time that separates these two pulses

is called the inter-pulse separation (Δt). The overall goal is to show that fiber deliverable laser pulses can (in combustion) delivery enough energy to ignite a lean air fuel mixture in a natural gas stationary engine (~10 to 20 mJ).

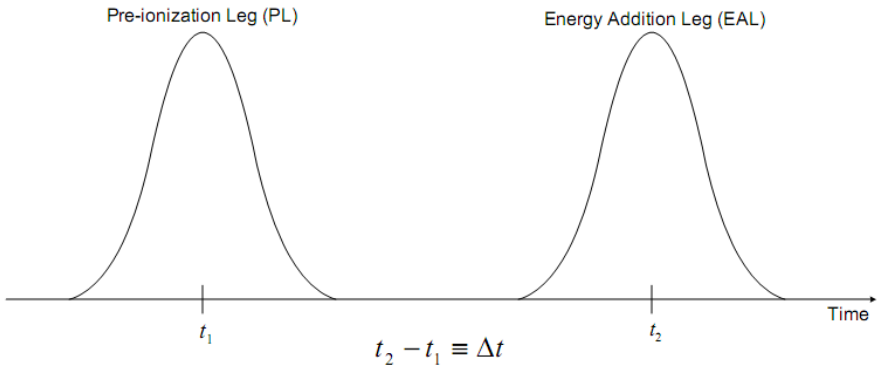

Figure 4.1: Basic principle of double pulse laser addition method.

The strategy with two pulses at the same wavelength was pursued because of the results from S. Hurandet al. recent work [50] with transmission of high peak power and high quality beam (almost single mode) through large core fibers at longer wavelengths compared to ultra-violet (UV). (The higher quality beam at the output of the fiber allows for tighter focusing of the beam to form sparks.)

Compared to UV light, transmission of infrared wavelength (1064 nm) via optical fibers to create sparks is more attractive. Our work with fiber optics has shown that higher output beam quality is possible at these longer wavelengths and there are lower chances of fiber damage[50]. Similarly, S. Hurandet al. have shown spark delivery through a 400 µm core fiber with 3-4 mJ pulse energy of 10 nanosecond 1064 nm light[50]. However, the energy needed for ignition

application is in the range of 10 – 20 mJ [10, 51]. The energy in the initial spark can be augmented by delivering energy via a second pulse. For instance the second pulse can be tailored to contain 10 – 30 mJ pulse energies but with longer duration such as 40 ns, so that the peak laser intensity is considerably less than the damage threshold of the fiber. The results of the parametric investigations of such energy addition process into a spark for a variety of conditions are presented.

In this chapter, experimental results from energy addition to a pre-ionized plasma volume using the dual pulse approach are presented. In Section 4.1, the experiment setup is presented. In Section 4.2, results and discussions of the dual pulse approach for energy addition are presented. In Section 4.3, two visualization technics are used to study the plasma evolution.

4.1 Experimental Setup

Figure 4.2 shows the two experimental setups that have been used for dual pulse energy addition process. The two laser beams used for the experiment were collinear. Figure 4.2a) shows the experimental setup where a single 1064 nm Nd:YAG laser (Big Sky, model) was used. The P-polarized beam was split into two legs. A thin film plate polarizer was used to convert one of the P-Polarized legs into S-polarized. The P-Polarized leg constituted formed a pre-ionization leg (PL) that made the spark or pre-ionized volume, and the S-Polarized leg formed the energy addition leg (EAL) that added the energy into the spark. The beam diameters for the two legs were controlled via telescopes in their respective

beam paths. The two beams were combined into a final beam via a recombiner (which let P polarized beam through and reflected S polarized beam). The final beam was focused by a plano-convex lens with a focal length of 20 mm. An extensive set of alignment procedures using infrared (IR) beam cards and charged coupled device (CCD) profiler (Spiricon, model) camera were used to ensure a high degree of spatial overlap between the two beams. Due to the limited space, this experimental setup provided a maximum inter-pulse separation of 40 nanoseconds between the two pulses legs. However, since a single laser source was used, any possible effects on the measurements due to different beam qualities and jitter were eliminated in this setup.

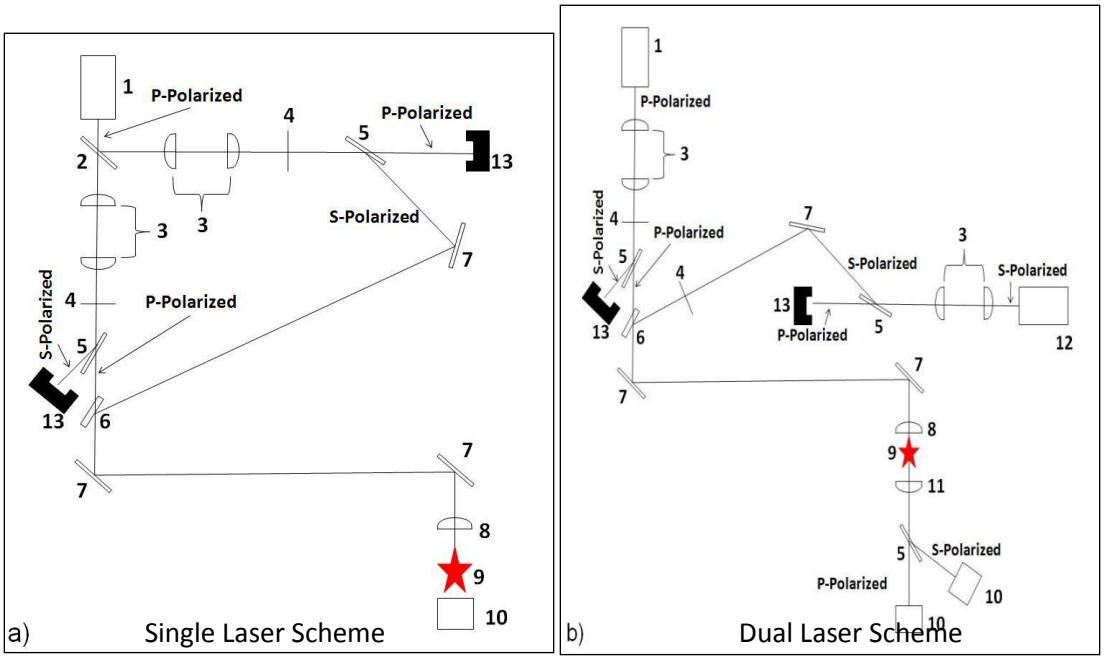

Figure 4.2: Schematic of the experimental setup used in the current work. 1) 1064 nm Nd:YAG laser (Big Sky Model), 2) 50/50 Beam Splitter, 3) Telescope, 4) Half Wave Plate, 5) Thin Film Plate Polarizer, 6) Recombiner, 7) Mirror, 8) Focusing Lens, 9) Spark Location, 10) Detector, 11) Collimating Lens, 12) 1064 nm Nd:YAG laser (Continuum Model) , 13) Beam Dump. The star indicates the location where the two beams are focused. Note: Different setups are used for different experiments and are referred to in the text.

Figure 4.2(b) shows the experimental setup where two different lasers were used so that a wide range of inter-pulse separation could be obtained. A 1064 nm Nd:YAG (Big Sky, model) with P polarized beam and a 1064 nm Nd:YAG (Continuum, model) with S polarized beam were used as the sources for the two legs. The beam qualities (M^2) of the two lasers were 1.8 and 3.7 respectively. The triggering of the two lasers was synchronized using a pulse delay generator. The Big Sky laser had a temporal jitter of ~10 ns. Similar to the first experimental setup, the two beams with two different polarizations were combined into one final beam using a beam recombiner (thin film polarizer).

In both experimental setups, the energy transmitted through the plasma was measured using an energy meter. Each leg had a variable attenuator formed by a combination of a half wave plate and a polarizer. The energy absorbed by the plasma was found as the difference between the input energy and the transmitted energy (measured just before/after the spark location). This procedure neglected any beam scattering or reflection from the laser spark. A thin film plate polarizer was placed after the spark in the dual-laser setup) so that the transmitted beam could be split into two beams corresponding to their polarization. This allowed for measurement of the energy deposited in the spark by each individual leg. The uncertainties (error bars) in the energy absorption measurements were found by laser temporal jitter (x-axis) and thermal energy meter (Ophir, model) highest and lowest values at that particular measurement (y-axis).

4.2 Results and Discussion

In this section, the results from the energy addition experiments are presented. First, the amount of energy that a spark from a single pulse would absorb at 100% sparking condition was investigated. Figure 4.3a shows the fraction of energy that is absorbed by spark at varying input energy levels. For this experimental configuration, the waist diameter at the focal position was 15 µm and the input laser energy at the spark threshold (i.e., when sparking is intermittent) was 5.5 mJ. The trend line in Fig. 4.3a shows that the fraction of energy absorbed by the spark remains nearly constant. This is consistent with other results which show that the fraction of energy absorbed by the spark grows linearly at energy levels just above the spark threshold and then remains constant at higher input energy levels [52].

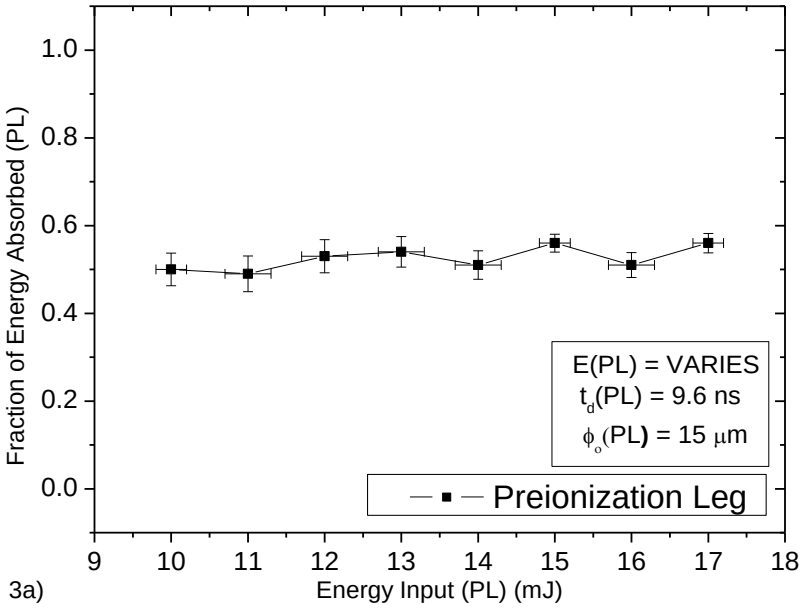

3a)

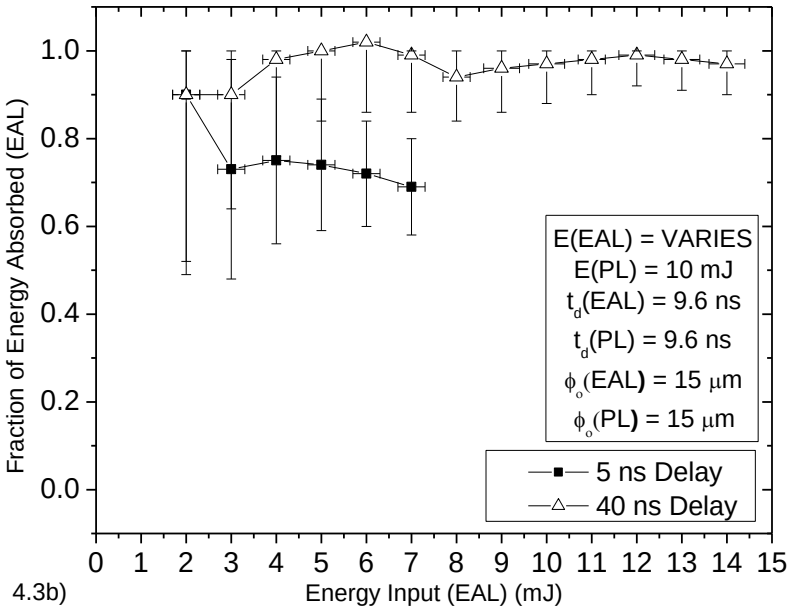

4.3b)

Figure 4.3: (a) Fraction of energy absorbed by the spark. (b) Fraction of energy absorbed by the spark from the energy addition leg (EAL) at 5 and 40 ns inter-pulse separations. The EAL and PL pulses are of equal diameter and duration.

Figure 4.3b shows the effect of two different inter-pulse separations of 5 and 40 ns on the fraction of energy that a spark formed by the first pulse (from the pre-ionizing leg) absorbs from the following pulse (energy addition leg). As shown in Fig. 4.2a, the beam from a single laser is split into two beams, recombined, and focused down to similar focal volumes with waist spot sizes of 15 µm thus eliminating effects of the jitter or beam quality on laser-plasma coupling. The energy in the pre-ionizing leg was held constant at 10 mJ whereas the energy in the energy addition leg was varied. At inter-pulse separation of 5 ns, the spark absorbs approximately 70% of the energy in the EAL. However, at 40 ns inter-pulse separation, within the measurement uncertainty, the spark completely absorbs the energy in the EAL.

Next, the effect of different focal spot sizes on the energy coupling between the spark and the following energy addition pulse were measured. In this set of experiments the beam in the pre-ionizing leg was focused to a waist diameter of 15 µm whereas the beam in the energy addition leg was focused to a waist diameter of 24 µm, hence the EAL beam did not spark on its own until 12mJ. Also consider that at 40 ns, the initial spark will have already grown to a size of ~1mm [53] and hence has a larger absorption cross-sectional area than the focused beam from the energy addition leg. Figure 4.4 shows that even with a larger spot size and 40 ns inter-pulse separation, the energy in the energy addition leg is completely absorbed by the spark (within experimental uncertainty).

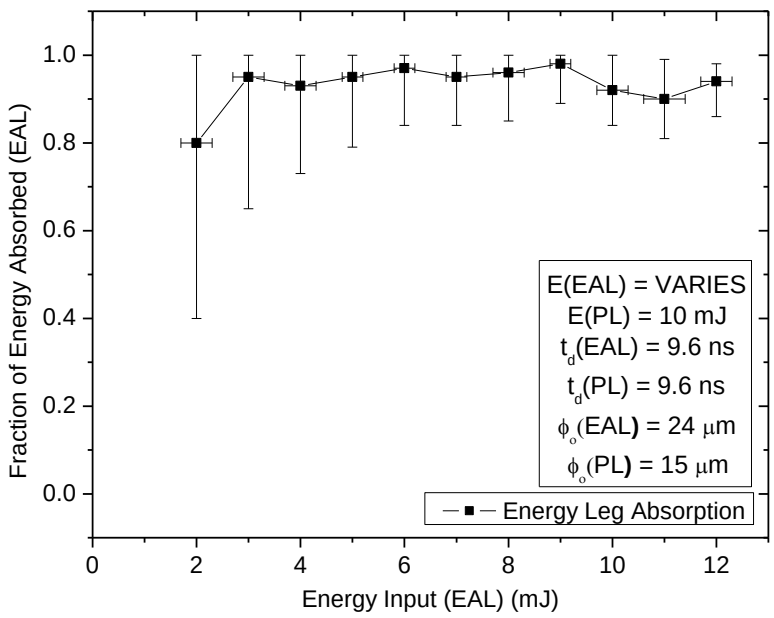

Figure 4.4: Fraction of energy absorbed by the spark from the energy addition leg (EAL) at 40 ns inter-pulse separation and with larger focused diameter of EAL.

Also, the investigation of the effect of longer inter-pulse separations (between the pre-ionizing and energy addition beam) on the energy coupling between the two beams in a focused volume was performed. The experimental setup in Fig. 4.2b was used to obtain the results that will be discussed below.

Figure 4.5 shows the fraction of energy a spark absorbs from the two legs when the pulses in the two legs are of similar duration (~10 ns). The energy in the preionizing leg and the energy addition leg are held constant at 13 and 16 mJ respectively. At 100% sparking condition and on their own (without the presence of other beam), the spark absorbs ~45% energy from the pre-ionizing leg and ~40% energy from the energy addition leg (within measurement uncertainties, absorptions are almost equal).

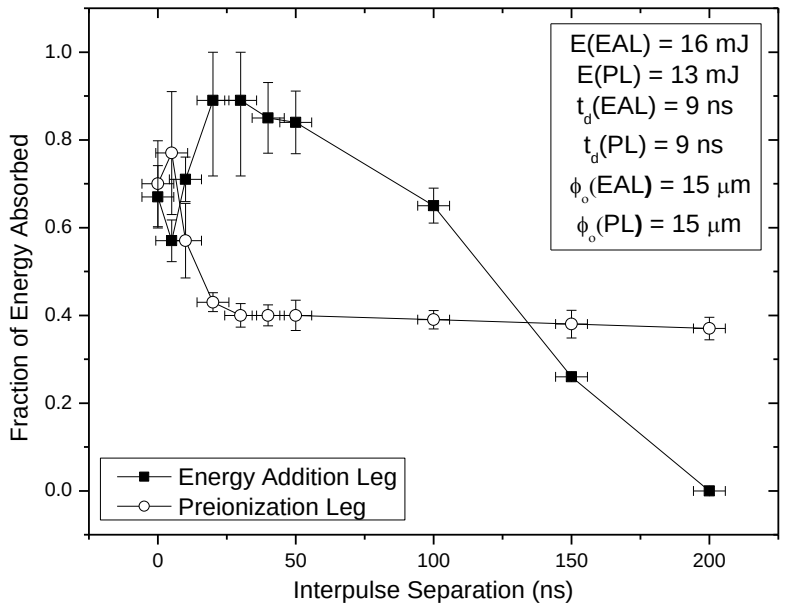

Figure 4.5: Fraction of energy absorbed by the spark from PL and EAL at various inter-pulse separations.

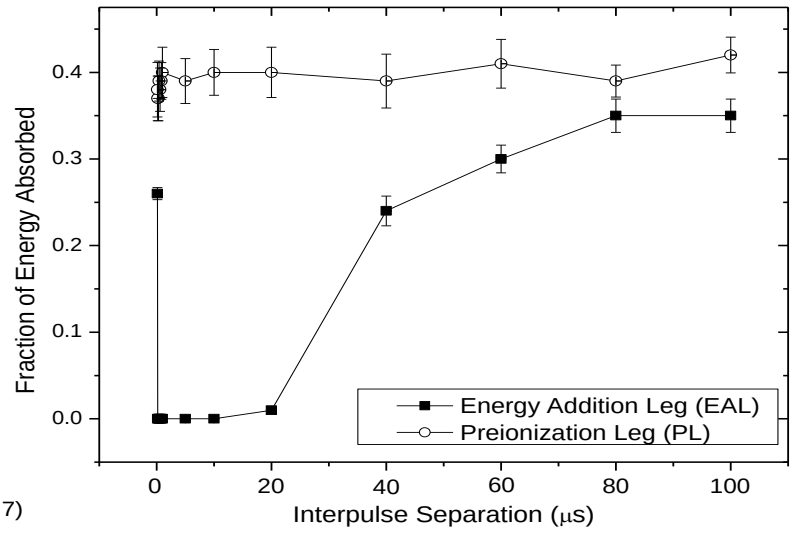

7)

Figure 4.6: Energy absorption behavior at conditions of Fig. 4.5 at much longer inter-pulse separations.

As shown in the Fig. 4.5, the fraction of energy absorbed by the spark from the energy addition leg increases from ~68% to ~90% at 20 – 40 ns (Within complete absorption measurement uncertainty). The ~20 ns delay before peak absorption could be the result of the dense initial plasma defocusing the EAL and in turn decreasing the intensity enough to stop the energy addition to the electron avalanche (by changing the index of refraction)[54].Another interesting observation is that the spark absorbs much higher fraction of energy from both legs at 0 ns (70% compared to the 40% - 45% when the two beam spark separately on their own). However, as shown in Fig. 4.6, the energy absorption coupling of the EAL by the plasma (first created by the PL) then drops off rapidly from 84% at 50 ns to 0% at 200 ns. As the inter-pulse separation is further increased from 200 ns to ~20-40 μs, the energy addition leg starts to exhibit intermittent sparking and shows 100% sparking only after 100 – 200 μs from the first pulse. The energy (in the energy addition leg) was increased from 16 to 25 mJ to investigate if it would make a difference and no significant difference was observed. The reduction on laser energy- plasma coupling (beginning at $\Delta t = 200$ ns) shows that the plasma becomes transparent to the subsequent laser pulse for a relatively long duration. Such a phenomenon where the laser becomes totally transmissive to the second pulse is also reported in reference [4, 5] and is attributed to the lowering of plasma absorption coefficient due to lower electron densities at time scales from ~200 ns onwards. (Note that a plasma is absorptive only when plasma frequency is equal or lower than laser frequency and at these time scales of 200 ns and onwards, plasmas can have lower

electron densities resulting in plasma frequency that is much lower than the laser frequency.) Another possibility for the transparency of the plasma could be contributed to the high temperature and low density at the waist location of the EAL [55]. Shneider et al. shows that at 100 ns the temperature and fractional density (plasma density/atmospheric density) at the center of the plasma is ~32,000 K and ~0.3 respectively, and at 30 μm the temperature drops to ~9,000 K and the fractional density approaches zero [56]. A detailed measurement of plasma temperature and electron densities at these time scales can provide a better understanding of the plasma state and the associated dip in absorption as seen in Fig. 4.5 and 4.6.

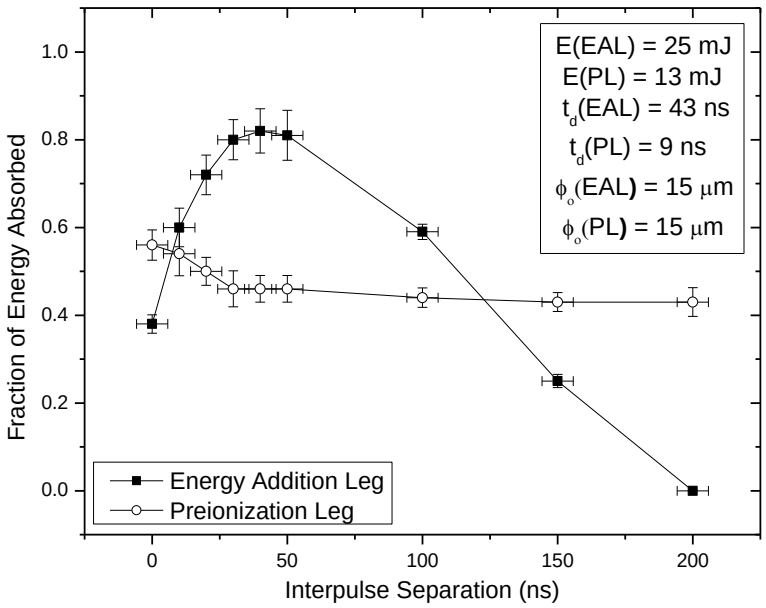

Figure 4.7: Fraction of energy absorbed by the spark at various inter-pulse separations and for longer pulse width in EAL.

Next, the effect of inter-pulse separation on the laser-plasma energy coupling when the pulse in the energy addition leg is significantly longer than the pre-ionizing pulse was investigated. Figure 4.7 shows the result of such an investigation. The pulse duration of the beams in the pre-ionizing leg and the energy addition leg are 9 and 43 ns respectively. The two beams are focused down to similar focal volumes with focal diameters of 15 µm. Similar to previous conditions (with short pulses in both legs), the spark absorbs ~ 82% energy from the energy addition leg at around 40 ns and then the absorption drops to 0% at around 200 ns. However in this experimental configuration, with different pulse durations (and temporal overlapping conditions) the spark absorbs lower amount of energy from each individual leg compared to the previous setup when two equal short pulses overlapped. For example, in the presence of longer pulse, only 57% energy from the pre-ionizing leg is absorbed by the spark (compared to around 71%-80% in the previous case when two short pulses overlapped temporally).

The ultimate goal is to show that one can send two pulses down a single large core and large cladding optical fiber (or more likely a double cladding fiber). In the case of a double cladding optical fiber the core would transmit the PL (to create the plasma/spark), and the first cladding would transmits the EAL to “feed” the plasma. Increasing the EAL’s pulse duration to 43 ns (as done in Fig. 4.7) would help keep the peak power lower than the optical fiber break down energy. The result of these conditions would produce a high power but very poor quality (M^2) beam that would not focus down enough to cause break down in

atmospheric air without a large amount of energy. Figure 4.8 shows the results of reenacting this type of situation. The setup is as shown in Fig. 4.2b, but the EAL was also passing through a silver coated hollow core fiber, as shown in Fig. 1.10 [13], to produce a poor quality beam (M^2=20-25). This would result in a much larger focal spot size that would cause break down in atmospheric air without a large amount of energy, and produced a spot size at the plasma location of 175 microns (compared to 30 microns with the PL). The PL and EAL durations are 9 and 43 ns respectively (same as Fig. 4.7), and the input energies are 14 and 34 mJ respectively. The results show that at the ideal 30-40 ns inter-pulse separation up to 87% of the energy was absorbed by the plasma. This produces approximately 37 mJ of total energy absorbed in the plasma, which 29.5 mJ of that energy comes from the EAL alone. This result indicate a possibility of using conventional multimode fiber optics to deliver energy adding second laser beam (with poor beam quality) into an already existing spark.

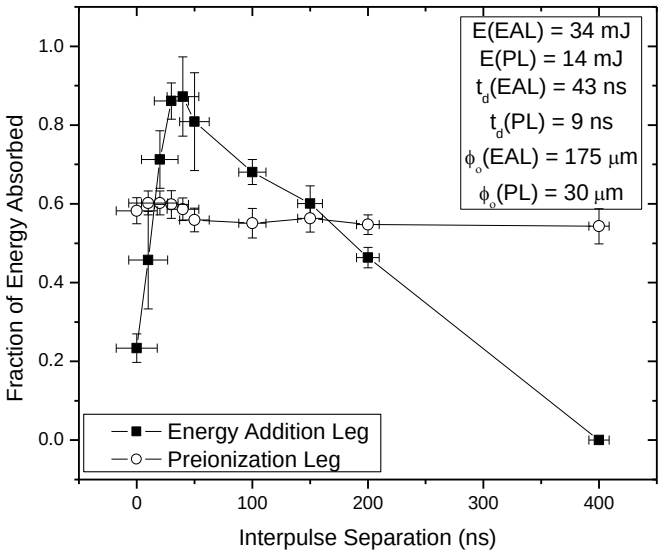

Figure 4.8: Fraction of energy absorbed by the spark at various inter-pulse separations and for longer pulse width and poor beam quality in EAL.

4.3 Plasma Evolution - Visualization

To visualize the formation and absorption of laser induced plasma, two techniques were explored: intensified charged coupled device (ICCD)to image the plasma formation and evolution and photo diode spectra to visualize energy absorption by the plasma. Other techniques have also been used to visualize plasma formation, for example: shadowgrams [57], laser probing (measuring the angle of deflection of a He-Ne laser as it travels through different depths of the plasma volume)[2], as well as microwave probing (such as RADAR REMPI)[58-60]. ICCD imaging has also been used in the past to visualize laser breakdown and subsequent plasma evolution [25].

4.3.1 Photo Diode Laser Pulse Tracing

Photo Diodes were used to look at how the energy from the EAL was absorbed by the spark. This was done by recording the pulse profile over time. Photo diodes were placed upstream and downstream of the spark. The upstream photo diode captured light scattered from a mirror, while the one placed downstream captured light scattered from an index card placed in the beam path. The signals from both photo diodes were captured in an oscilloscope and then transferred into a computer using a LabVIEW program. Figure 4.9 and 4.10 show the laser pulse spectra for single pulse (PL only), and dual pulse with 36 ns inter-pulse separation respectively. Figure 4.9 clearly shows the breakdown and laser absorption by the spark. When the pulse energy reaches a critical threshold there is a sharp drop indicating the absorption of the pulse by the spark. Approximately 55% of the energy in the pulse is absorbed by the spark. In Fig. 4.10, two pulses from PL and EAL are shown. Two peaks from the PL and EAL are clearly shown for the pulses before the spark. However, once the plasma is formed by the PL leg, almost all (~87%) of the energy from the EAL leg is absorbed by the spark.

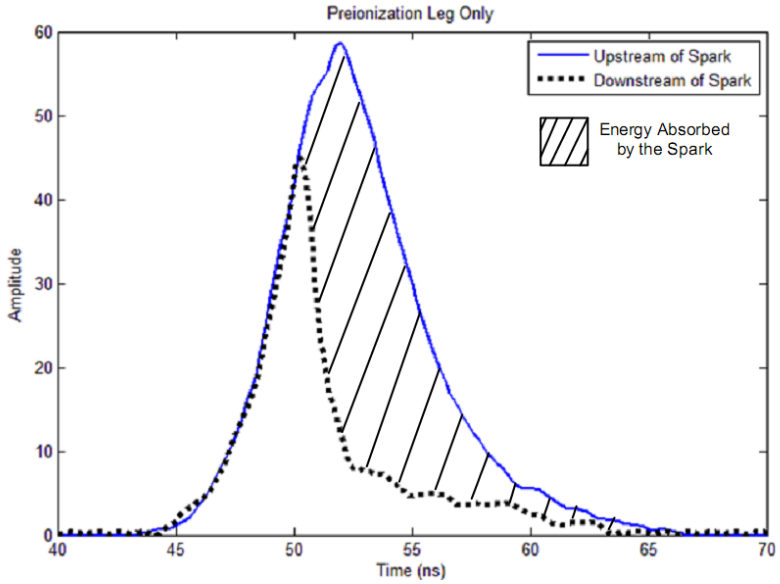

Figure 4.9: Spectra taken with two photo diodes (up and downstream of spark location) for single pulse (PL only).

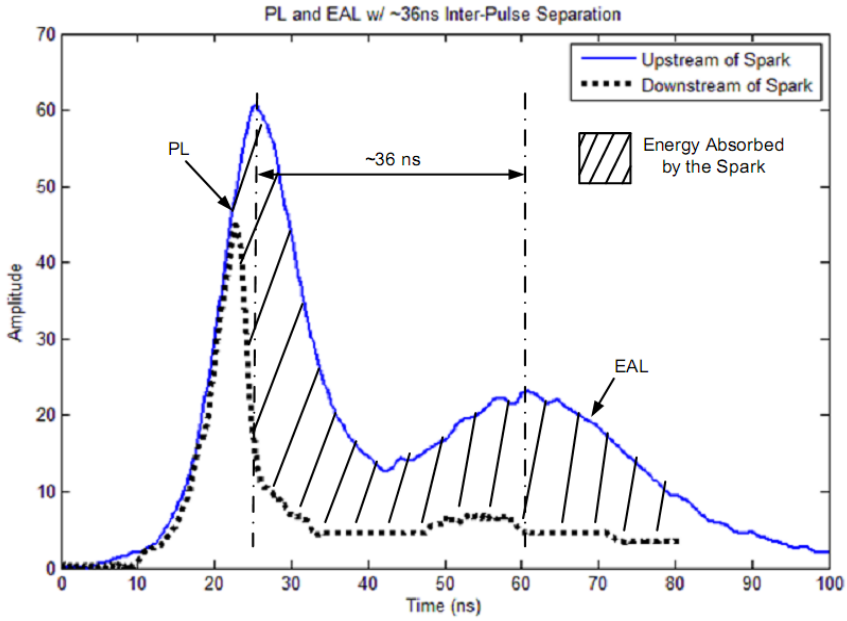

Figure 4.10: Spectra taken with two photo diodes (up and downstream of spark location) for dual pulse (both PL and EAL) with ~36 ns inter-pulse separation.

4.3.2 Plasma Visualization Using ICCD

As stated earlier, ICCD have been used to visualize plasma evolution. In this section the ICCD images are used to compare the differences in plasma evolution resulting from a single pulse and dual pulse with laser propagating from left to right (Figure 4.11). The ICCD camera (DiCAM-PRO) was placed perpendicular to the optical beam path and focused at the spark location and the camera was synchronized with the laser. The first column (a) shows plasma evolution for single pulse, while the second (b) and third (c) column shows plasma evolution for dual pulse with 0 and 40 ns inter pulse separation (Δt) respectively. The images show that the plasma evolves similarly for single pulse and dual pulse with$\Delta t = 40$ ns. This is due to the fact that only 20 to 30% of the EAL is being absorbed by the spark. However, when inter-pulse separation is 40 ns 80 to 90% is absorbed and hence the plasma is larger. The gain was changed between images to avoid saturation, which allows one to approximate the plasma size. Note, because of different gain settings, the images cannot be compared with each other for relative intensity (which may provide temperature information). The threshold was set visually when the images were taken. The images were processed with Photoshop (to remove the background) and MATLAB. MATLAB was used to count the number of pixels in the plasma of each image. Then by applying a conversion factor to change number of pixels to area (mm^2), a graph can be produced that shows the area of the plasma over time (Figure 4.12). This graph mimics what is seen in the ICCD images. Both the single pulse and dual pulse with $\Delta t = 0$ ns show similar curves with an

average difference of ~0.2 mm^2. While the difference between single pulse and dual pulse with $\Delta t = 40$ ns delay is ~2.1 mm^2. The larger volume of the plasma at later times (such as 5 µs) obtained with 40 ns inter-pulse delay may provide a better ignition source than small plasma volumes in terms of resistance to quenching, higher fraction of reactants, larger flame front area etc.

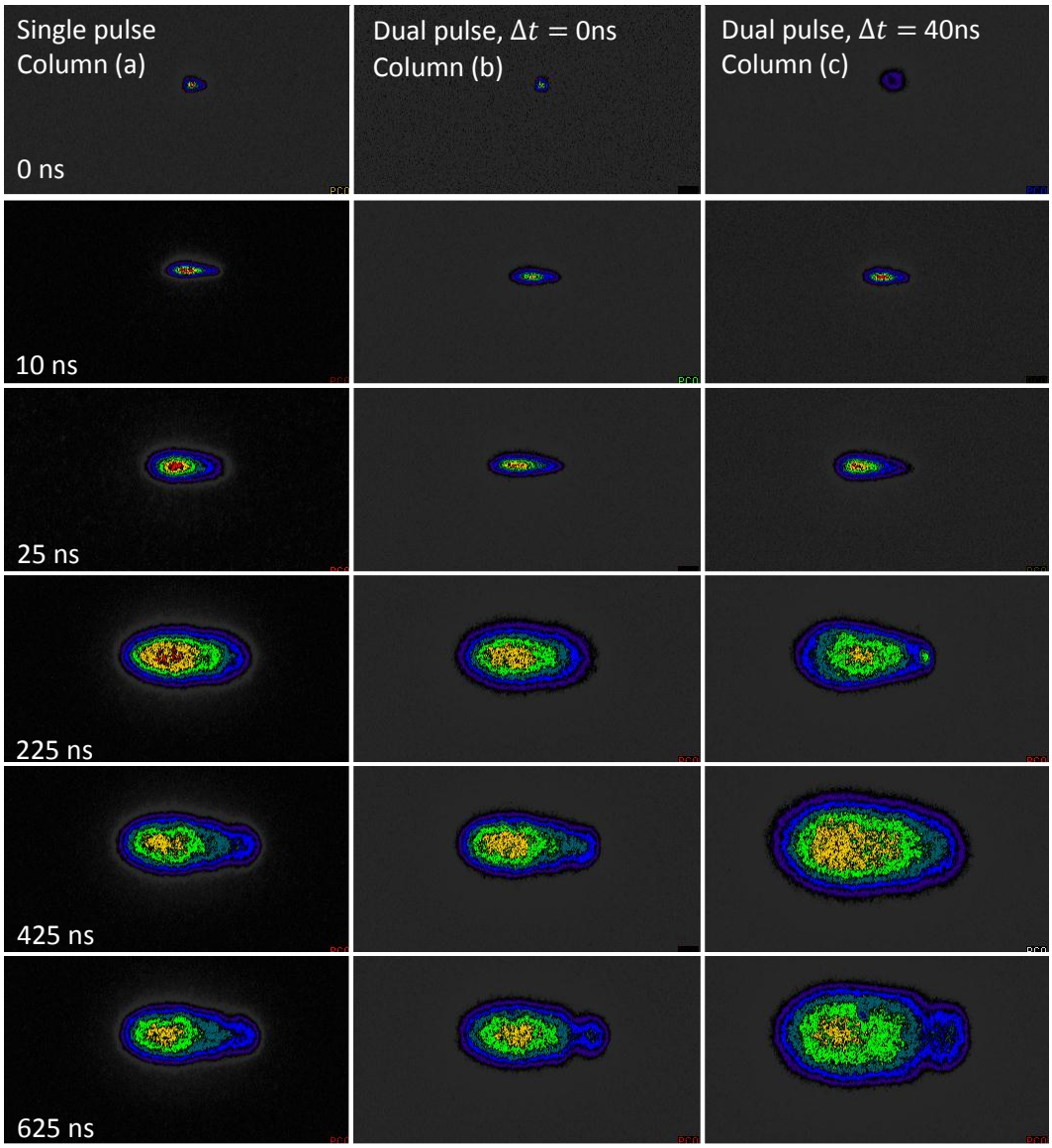

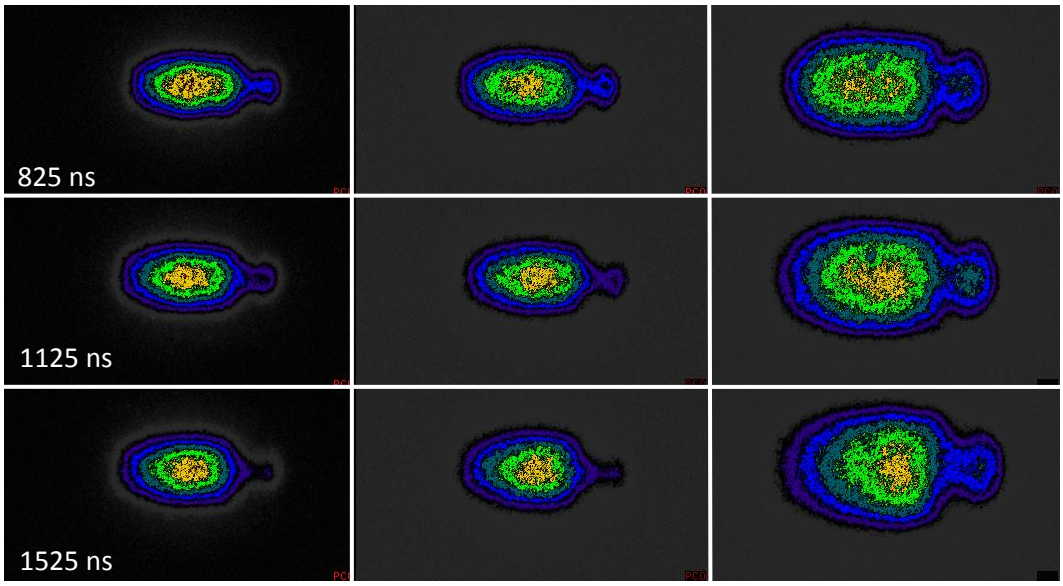

Figure 4.11:Difference in evolution of the plasma between single (a) and dual pulse air breakdown for both 0 (b) and 40 (c) ns inter-pulse separation (Δt). Note: laser settings the same as for Figure 4.9 andthe gain was varied between each image. Also laser propagation is form left to right.

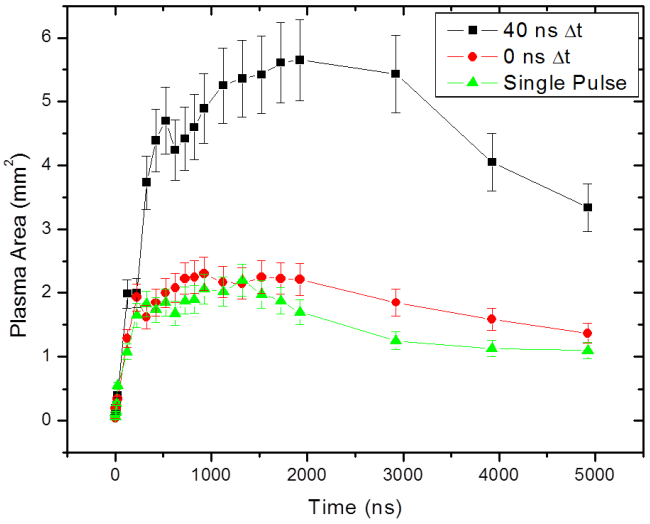

Figure 4.12: Measured area (mm^2) of plasmas for single and dual laser pulses at different times (ns).

Chapter 5

CONCLUSIONS AND FUTURE WORK

Laser ignition is a potential ignition technology for advanced natural gas engines; however, the optimum ignition configuration, e.g., use of open chamber laser plug or non-fueled laser prechamber plug, depends on the engine operation and design. In this research, tests were conducted on a Caterpillar G3516C engine with a non-fueled electric prechamber plug, a non-fueled laser prechamber plug, and an open chamber laser plug. Test data showed that the open chamber laser plug exhibited a high degree of combustion instability. On the other hand, the performance of the electric prechamber plug and laser prechamber plug were very comparable, although small differences such as a lower degree of combustion variability for the electric prechamber were observed. Nonetheless, test data for the laser prechamber plug showed the capability of the laser sparks (and associated early flame kernels) to withstand non-ideal flow field conditions within the prechamber.

It was hypothesized that the higher combustion variability observed with the laser prechamber plug is due to: i) high flow velocities and turbulence at the laser spark location (in the middle of the prechamber), ii) lower prechamber volume of LPP compared to EPP, and iii) possible non-optimum fuel air ratio at

the spark location. To help understand the turbulent flow inside the optical prechamber, computational fluid dynamics CFD was employed.

The CFD found that to optimize the use of the optical prechamber the spark should be located in the bottom half of the prechamber to reduce the quenching due to turbulence. Future work should concentrate on expanding the mesh to include the main chamber. This could be done simply by applying a UDF pressure curve to a stationary main cylinder to mimic the flow between the two chambers. This would require less computing time without the use needing to assume azimuthal symmetry. Furthermore, instead of air, use of air-fuel mixtures during the simulation would give a more complete picture of fuel-air ratio distribution within the prechamber. In order to capitalize on the benefits of laser sparks, and to achieve superior combustion, one should investigate a re-designed prechamber with optimized spark location.

Other experiments conducted as part of this research have shown that it is possible to increase the energy of the laser spark by employing a dual laser pulse method. The first pulse initiates the spark while the second pulse deposits additional energy into the spark. It was shown that the initial spark can absorb 80 to 90% energy of the second pulse if the inter-pulse separation (Δt) is about 20 to 40 nanoseconds. At an inter-pulse separation of 200 ns the plasma appeared transparent to the second pulse. This could be explained by the rapid decrease of electron density (which in turn a rapid decrease in plasma frequency). It was also shown that even with a poor quality ($M^2 \approx 25$) beam, which was loosely focused creating a large waist ($175\mu m$), and long pulse

duration (~42ns) that one still has large absorption of ~90% for appropriate pulse delays. This result shows the possibility of using a dual pulse approach in which a first pre-ionizing pulse is delivered through a small core fiber to form the spark, and a second pulse of large energy is delivered through a large clad (poor beam quality) fiber for subsequent energy addition.

REFERENCES

[1] D. Bradley*, et al.*, "Fundamentals of high-energy spark ignition with lasers," *Combustion and Flame,* vol. 138, pp. 55-77, 2004.

[2] T. X. Phuoc, "An experimental and numerical study of laser-induced spark in air," *Optics and Lasers in Engineering,* vol. 43, pp. 113-129, 2005.

[3] Y.-L. Chen and J. W. L. Lewis, "Visualization of laser-induced breakdown and ignition," *Opt. Express,* vol. 9, pp. 360-372, 2001.

[4] V. Hohreiter*, et al.*, "Temporal analysis of laser-induced plasma properties as related to laser-induced breakdown spectroscopy," *Spectrochimica Acta Part B: Atomic Spectroscopy,* vol. 59, pp. 327-333, 2004.

[5] P. K. Diwakar and D. W. Hahn, "Study of early laser-induced plasma dynamics: Transient electron density gradients via Thomson scattering and Stark Broadening, and the implications on laser-induced breakdown spectroscopy measurements," *Spectrochimica Acta Part B: Atomic Spectroscopy,* vol. 63, pp. 1038-1046, 2008.

[6] V. I. Babushok*, et al.*, "Double pulse laser ablation and plasma: Laser induced breakdown spectroscopy signal enhancement," *Spectrochimica Acta Part B: Atomic Spectroscopy,* vol. 61, pp. 999-1014, 2006.

[7] L. St-Onge*, et al.*, "Analysis of solids using laser-induced plasma spectroscopy in double-pulse mode," *Spectrochimica Acta Part B: Atomic Spectroscopy,* vol. 53, pp. 407-415, 1998.

[8] A. P. Yalin*, et al.*, "Laser Ignition of Natural Gas Engines Using Fiber Delivery," *ASME Conference Proceedings,* vol. 2005, pp. 633-641, 2005.

[9] S. Joshi*, et al.*, "Laser-Induced Breakdown Spectroscopy for In-Cylinder Equivalence Ratio Measurements in Laser-Ignited Natural Gas Engines," *Appl. Spectrosc.,* vol. 63, pp. 549-554, 2009.

[10] S. Joshi*, et al.*, "On Comparative performance testing of prechamber and open chamber laser ignition," in *ICEF 2010-35058 , 2010 ASME Internal Combustion Engine Fall Technical Conference*, 2010.

[11] S. Joshi*, et al.*, "Temperature and Electron Density Measurements of Laser Induced Plasmas in Air at Elevated Pressures," Spectroscopy Letters, 2010.

[12] A. P. Yalin*, et al.*, "Towards Multiplexed Fiber Delivered Laser Ignition for Natural Gas Engines," *Journal of Engineering for Gas Turbines and Power,* vol. 130, pp. 044502-4, 2008.

[13] A. P. Yalin*, et al.*, "Use of hollow-core fibers to deliver nanosecond Nd:YAG laser pulses to form sparks in gases," *Opt. Lett.,* vol. 30, pp. 2083-2085, 2005.

[14] G. Herdin*, et al.*, "Laser Ignition: A New Concept to Use and Increase the Potentials of Gas Engines," *ASME Conference Proceedings,* vol. 2005, pp. 673-681, 2005.
[15] M. Weinrotter*, et al.*, "Laser-Ignition of Methane-Air Mixtures at High Pressures and Temperatures," in *European Combustion Meeting*, Jenbach, Austria, 2005.
[16] J. B. Heywood, *Internal combustion engine fundamentals*. New York: McGraw-Hill, 1988.
[17] H. M. Cho and B.-Q. He, "Spark ignition natural gas engines--A review," *Energy Conversion and Management,* vol. 48, pp. 608-618, 2007.
[18] G. Herdin*, et al.*, "GE Jenbacher's Update on Laser Ignited Engines," *ASME Conference Proceedings,* vol. 2006, pp. 475-481, 2006.
[19] S. F. Adams*, et al.*, "Resonant Laser Induced Breakdown for Fuel-Air Ignition," in *48th AIAA Aerospace Sciences Meeting*, Orlando, Florida, 2010.
[20] T. X. Phuoc and F.P.White, "Laser-Induced Spark Ignition of CH4/Air Mixtures," *Combustion and Flame,* vol. 119, pp. 203-216, 1999.
[21] I. C. E. Turcu*, et al.*, "Measurement of KrF laser breakdown threshold in gases," *Optics Communications,* vol. 134, pp. 66-68, 1997.
[22] J. P. Davis*, et al.*, "Laser-induced plasma formation in Xe, Ar, N2, and O2 at the first four Nd:YAG harmonics," *Applied Optics,* vol. 30, pp. 4358-4364, 1991.
[23] R. Tambay and R. K. Thareja, "Laser-induced breakdown studies of laboratory air at 0.266, 0.355, 0.532, and 1.06 mu m," *Journal of Applied Physics,* vol. 70, pp. 2890-2892, 1991.
[24] G. V. Ostrovskaya and A. N. Zaĭdel, "Laser spark in gases," *Soviet Physics Uspekhi,* vol. 16, 1974.
[25] N. Glumac and G. Elliott, "The effect of ambient pressure on laser-induced plasmas in air," *Optics and Lasers in Engineering,* vol. 45, pp. 27-35, 2007.
[26] Ş. Yalçin*, et al.*, "In uence of ambient conditions on the laser air spark," *Applied Physics B: Lasers and Optics,* vol. 68, p. 121, 1999.
[27] S. Joshi*, et al.*, "A Time Resolved Spectroscopic Study of Laser Generated Plasmas in Air at High Pressures," presented at the AIAA, 2010.
[28] D. Bradley*, et al.*, "The Measurement of Laminar Burning Velocities and Markstein Numbers for Iso-octane-Air and Iso-octane-n-Heptane-Air Mixtures at Elevated Temperatures and Pressures in an Explosion Bomb," *Combustion and Flame,* vol. 115, pp. 126-144, 1998.
[29] H. Kopecek*, et al.*, "Laser ignition of methane-air mixtures at high pressures," *Experimental Thermal and Fluid Science,* vol. 27, pp. 499-503, 2003.
[30] A. Sircar*, et al.*, "Laser induced breakdown of Ar, N₂ and O₂ gases using 1.064, 0.532, 0.355 and 0.266 μm radiation," *Applied Physics B: Lasers and Optics,* vol. 63, pp. 623-627, 1996.

[31] G. Kroupa*, et al.*, "Novel miniaturized high-energy Nd-YAG laser for spark ignition in internal combustion engines," *Optical Engineering,* vol. 48, pp. 014202-5, 2009.
[32] D. L. McIntyre*, et al.*, "Lean-Burn Stationary Natural Gas Engine Operation With a Prototype Laser Spark Plug," *Journal of Engineering for Gas Turbines and Power,* vol. 132, pp. 072804-6, 2010.
[33] S. Joshi*, et al.*, "Use of hollow core fibers, fiber lasers, and photonic crystal fibers for spark delivery and laser ignition in gases," *Appl. Opt.,* vol. 46, pp. 4057-4064, 2007.
[34] S. Hurand*, et al.*, "Mode Coupling and Output Beam Quality of 100-400 Micrometer Core Silica Fibers," unpublished.
[35] A. E. Siegman, "Defining, measuring, and optimizing laser beam quality," Los Angeles, CA, USA, 1993, pp. 2-12.
[36] S. Joshi, "manuscript in preperation," 2011.
[37] M. E. Crane and S. R. King, "Emission Reductions through precombustion chamber desing in a natural gas, lean burn engine," *Transactions of the ASME,* vol. 114, pp. 466-474, 1992.
[38] R. P. Roethlisberger and D. Favrat, "Comparision between direct and indirect (prechamer) spark ignition in the case of a cogeneration natural gas engine, part II : engine operating parameters and turbocharger characteristics," *Applied Thermal Engineering,* 2002.
[39] J. B. Heywood, *Internal Combustion Engine Fundamentals*, 1988.
[40] R. P. Roethlisberger and D. Favrat, "Investigation of the prechamber geometrical configuration of a natural gas spark ignition engine for cogeneration: part I. Numerical simulation," *International Journal of Thermal Sciences,* vol. 42, pp. 223-237, 2002.
[41] S. J. Charlton*, et al.*, "Computer Modeling and Experimental Investigation of a Lean Burn Natural Gas Engine," *SAE Paper No. 900228*.
[42] R. Tambay and R. K. Thereja, "Laser-induced breakdown studies of laboratory air at 0.266, 0.355, 0.532, and 1.06 μm," *J. Appl. Phys.,* vol. 70, pp. 2890-2892, 1991.
[43] A. N. Laboratory, "DOE - Round table Ignition Meeting," Argonne National Laboratory2009.
[44] C. C. Huang*, et al.*, "A transition on minimum ignition energy for lean turbulent methane combustion in flamelet and distributed regimes," *Proceedings of the Combustion Institute,* vol. 31, pp. 1401-1409, 2007.
[45] S.-C. Kong, "A study of natural gas/DME combustion in HCCI engines using CFD with detailed chemical kinetics," *Fuel,* vol. 86, pp. 1483-1489.
[46] I. G. Dors and C. G. Parigger, "Computational Fluid-Dynamic Model of Laser-Induced Breakdown in Air," *Appl. Opt.,* vol. 42, pp. 5978-5985, 2003.
[47] D. Wunsch*, et al.*, "NUMERICAL FLOW SIMULATION OF A NATURAL GAS ENGINE EQUIPPED WITH AN UNSCAVANGED AUTO-IGNITION PRECHAMBER," in *Proceedings of the European Combustion Meeting*, Lausanne, Switzerland, 2007.

[48] V. Yakhot*, et al.*, "Development of turbulence models for shear flows by a double expansion technique," *Physics of Fluids A: Fluid Dynamics,* vol. 4, pp. 1510-1520, 1992.
[49] H. K. Versteeg and W. Malalasekera, *An Introduction to Computational Fluid Dynamics: The Finite Volume Method*. England: Pearson Education Limited, 1995.
[50] S. Hurand*, et al.*, "Mode Coupling and Output Beam Quality of 100-400 Mircrometer Silica Core Fibers," *In preparation,* 2010.
[51] H. Kopecek*, et al.*, "Laser Ignition of Methane-Air Mixtures at High Pressure and Diagnostics," *Jnl. of Eng. for Gas Turb. and Power,* vol. 127, pp. 213-219, 2005.
[52] H. El-Rabii*, et al.*, "Properties of an air plasma generated by ultraviolet nanosecond laser pulses," *J.Phys.D : Appl. Phys.,* vol. 42, pp. 1-10, 2009.
[53] V. Hohreiter*, et al.*, "Temporal Analysis of laser-induced plasma properties as related to laser-induced breakdown spectroscopy," *Spectrochemica Acta part B,* vol. 59, pp. 327-333, 2004.
[54] C. V. Bindhu*, et al.*, "Energy Absorption and Propagation in Laser-Created Sparks," *Appl. Spectrosc.,* vol. 58, pp. 719-726, 2004.
[55] Z. Zhang*, et al.*, "Diagnostics by RADAR REMPI: Microwave Scattering from Laser-induced Small-volume Plasmas," *American Institute of Aeronautics and Astronautics,* 2006.
[56] M. N. Shneider, "Turbulent decay of after-spark channels," *Physics of Plasmas,* vol. 13, pp. 073501-11, 2006.
[57] M. Villagran-Muniz*, et al.*, "Shadowgraphy and interferometry using a CW laser and a CCD of a laser-induced plasma in atmospheric air," *Plasma Science, IEEE Transactions on,* vol. 29, pp. 613-616, 2001.
[58] Z. Zhang*, et al.*, "Experiments on Microwave Scattering of REMPI in Argon, Xenon, and Nitric Oxide," in *38th AIAA Plasmadynamics and Lasers Conference*, Miami, FL, 2007.
[59] Z. Zhang*, et al.*, "*Temperature measurement of Nitric oxide by Radar REMPI*." 46th AIAA Aerospace Sciences Meeting and Exhibit, 2008.
[60] Z. Zhang and M. N. Shneider, "Measurement of Plasma Decay Processes in Mixture of Sodium and Argon by RADAR REMPI," in *AIAA*, San Antonio TX, 2009.